Quantum Electronics **36** (9) 801 – 820 (2006)

REVIEW

PACS numbers: 42.79.Qx; 42.68.Wt; 42.62.Cf
DOI: 10.1070/QE2006v036n09ABEH006577

IR differential-absorption lidars for ecological monitoring of the environment

B.I. Vasil'ev, O.M. Mannoun

Contents

***Abstract*. A review of studies on lidar sensing of the environment by the method of IR differential absorption is presented. The differential-absorption method is described and its various applications are considered. A comparison of this method with other methods of lidar sensing showed that a differential-absorption lidar successfully supplements a Raman lidar. The basic parameters are presented for IR lidars fabricated recently by various research groups. The outlook for the IR lidar sensing of the atmosphere is discussed.**

Keywords: *IR differential-absorption lidar, atmosphere, pollutants, Freons, dioxins, solid-state lidars, He – Ne laser, DF lidar, CO_3 lidar, NH_3 lidar.*

B.I. Vasil'ev P.N. Lebedev Physics Institute, Russian Academy of Sciences, Leninsky prosp. 53, 119991 Moscow, Russia;
e-mail: bvasil@sci.lebedev.ru;
O.M. Mannoun Moscow Institute of Physics and Technology (State University), Institutskii per. 9, 141700 Dolgoprudnyi, Moscow region, Russia

Received 17 March 2005; revision received 13 December 2005
Kvantovaya Elektronika **36** (9) 801 – 820 (2006)
Translated by M.N. Sapozhnikov

1. Introduction

Intensive remote sensing studies have shown that a lidar is one of the most promising instruments for studying the atmosphere and monitoring its pollution [1 – 3]. Recently lidars have been widely used in various fields of science and technology, especially for ecological monitoring of the atmosphere. The main direction of the development of lidar sensing is the refinement of the methods of differential absorption (DA) [2, 4] and Raman scattering [5, 6]. The best results were obtained with IR differential-absorption lidars (DIALs), especially operating in the spectral region from 2.5 to 14 μm. The isolated intense absorption lines of almost all atmospheric gases and pollutants are located in this region [7]. In addition, emission lines of some efficient and high-power lasers such as DF, CO, CO_2, and NH_3 lasers lie in this region.

The DA method was first proposed and realised in practice by Schotland in 1964 for laser sensing of the water vapour in the atmosphere. Schotland called this method the method of 'differential absorption of scattered energy' (DASE). Also, the terms 'differential-absorption lidar' (DIAL), 'differential absorption and scattering' (DAS) or simply 'method of differential absorption' are used [1, 2]. The method is based on the resonance absorption of laser

radiation within the absorption line profile of a gas under study. The gas concentration is calculated by using signals at two close frequencies, one of which is located within the absorption line and another outside it. DIALs are widely used for measuring concentrations of gases such as NO_2, SO_2, H_2O, C_2H_2, NH_3, and O_3 with a sensitivity threshold of 1ppb (1 billion^{-1}) [8]. To probe all the pollutants by this method, several lasers are required covering a broad UV–IR spectral range, which complicates the realisation of such a system [1, 2]. In addition, some gases have very narrow absorption lines and, therefore, their DA sensing requires the use of tunable lasers emitting narrow enough and very stable lines.

One of the most interesting fields of lidar sensing is the use of femtosecond lidars for sensing [9]. The use of a high-power femtosecond laser emitting 400-mJ, 80-fs pulses with a pulse repetition rate of 10 Hz [10] opens up new prospects in the field of atmosphere sensing. Such lasers can initiated a breakdown in a gas, producing plasma emitting radiation with a broad spectrum in the region from 0.3 to 4.5 μm. Such a broadband radiation allows the simultaneous monitoring of many gases such as methane, water vapour, SO_2, etc. In addition, femtosecond lasers allow one to identify various aerosols in the atmosphere.

2. Features of lidar sensing of the atmosphere

It is known that the most complete information about the composition and state of the atmosphere with a high spatiotemporal resolution and sensitivity can be obtained only by the optical method by using lidars [1–3]. The term lidar is the abbreviation of the expression 'light identification, detection and ranging'.

Most of the lidars consist of three basic parts: transmitting, receiving, and control systems. Figure 1 shows the elements and operation principle of lidars. The transmitting part of the lidar usually contains a laser and an optical system for formation of the output laser beam, i.e. for controlling the output spot size and divergence of the laser beam. Radiation scattered in the volume under study is collected with a telescope and is detected with a high-sensitive photodetector. The lidar should also contain an element performing the frequency discrimination of the received signals. This element separates radiation at the specified wavelength from the received signal. Such an element can be a narrowband interference filter with a high noise rejection level or a monochromator in some cases. Optical signals are digitised and processed and stored in a computer [1–3].

Lidar systems are divided according to their design into bistatic and monostatic. The radiation source and receiver in a bistatic (path) lidar are located on the opposite sides of the object under study. This instrument is intended for continuous monitoring the state of the atmosphere in a specified direction in open-cut mines, regions of oil wells, etc. A monostatic lidar is completely based in one place (stationary, automobile chassis, helicopter- or airborne, and spaceborne). The probe radiation is returned by using either Mie scattering or a mirror or reflection from natural topographic objects such as buildings, trees, the surface of earth or water. Such lidars are very mobile and can be used to study widespread area. The most efficient is a monostatic lidar in which radiation is returned by using various optical processes occurring in the object under study itself. In this case, it is possible not only to determine the composition of contaminations in the atmosphere but also to find the distance to the object from the delay of the reflected light pulse from the initial laser pulse. Lidar systems are also divided into monoaxial and biaxial according to the type of the transmitting and (or) receiving parts. The objective of a telescope in a monoaxial lidar operates simultaneously as the transmitting and receiving parts. In a biaxial laser, these parts are separated and the distance between the axes of these parts is its base.

The transmitting part of the lidar consists of one or several lasers and an optical system. A high-power laser pulse at one or several frequencies is corrected by a transmitting optical system and is directed to a target.

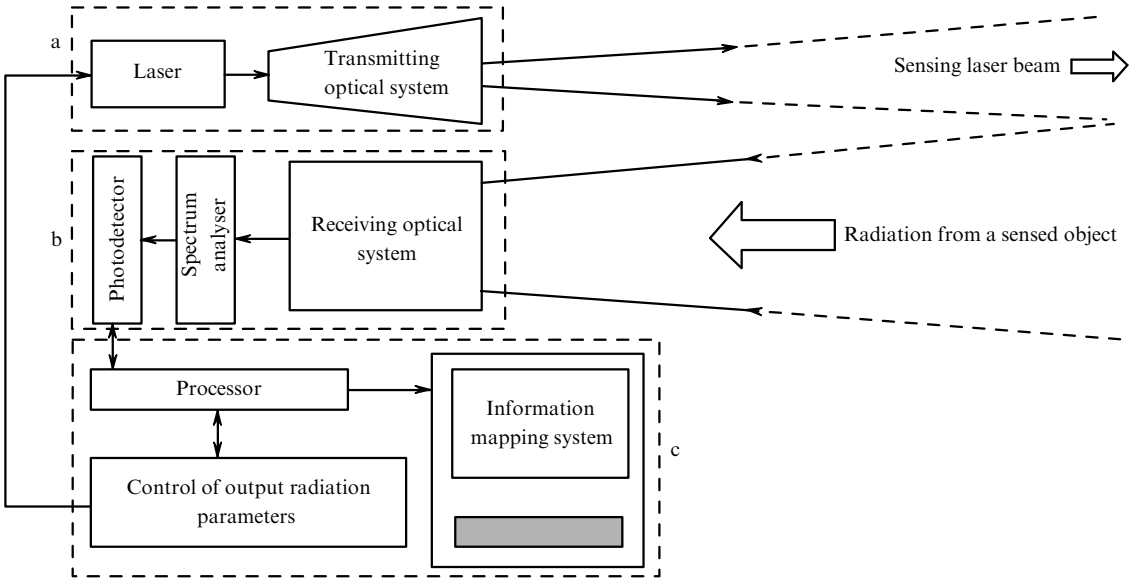

Figure 1. Principal scheme of a lidar: transmitting part (a), receiving part (b), and control system (c).

The transmitting system should solve three problems: to improve the collimation of the light beam, to perform the spatial filtration of the beam and reject any undesirable radiation, including the side radiation of the lasers. Note that the initial part of the laser pulse is sometimes specially modulated to indicate the instant of the beginning of time measurements and to normalise the intensity of the useful signal. The normalisation is performed in the case of a poor reproducibility of the input-pulse parameters and also to control the laser wavelength when necessary.

The receiving part consists of an objective (telescope), a spectral and (or) spatial filters, a polarisation element, and a photodetector. Usually, mirror objectives are employed, of which the most popular are the Newton, Gregory, and Cassegrain objectives. Radiation reflected and scattered from the object under study is concentrated by a receiving optics (telescope) and passes through a spectrum analyser. This instrument separates the wavelength range in which observations are performed by rejecting background radiation at other wavelengths. A spectrum analyser can be either a carefully adjusted monochromator or polychromator or a set of narrowband filters, including a filter rejecting radiation at the laser transmitter wavelength. The latter is used in the case when resonantly scattered light is not analysed.

The system for control, data detection and processing performs the following functions:

(i) control of the lidar operating regime;

(ii) control of the probe laser radiation frequency;

(iii) measurements of the energy of the output and received two-frequency laser beams at both frequencies;

(iv) processing of the results, i.e. the determination of the spectral characteristics of the atmosphere and the measurement of the concentration of contaminations by using the 'spectral portraits' of molecules contained in the data base in the computer;

(v) control of the lidar guidance system.

Figure 2 shows the structural diagram of the lidar control system in which directing to an object is performed with a video camera. In [11–15], various technical characteristics and elements of lidars were studied: the dynamic range and methods for its compression, spatial filters, receiving objectives, analysers of the polarisation state, etc.

The interaction of laser radiation with the atmosphere is characterised by various physical processes. The modern methods of laser sensing are based on Rayleigh, Raman, and Mie scattering, fluorescence, absorption, and differential absorption and scattering. These methods are described in [2], and we present below their comparative characteristics.

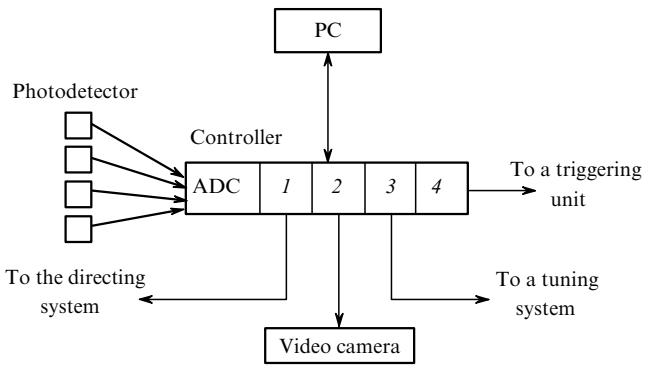

Figure 2. Structural scheme of the control, recording, and processing system of the lidar information: (*1*) amplifier of the directing system drivers; (*2*) unit for video camera – PC coupling; (*3*) control unit for a step motor for laser tuning; (*4*) synchroniser for the laser triggering unit.

Raman scattering can be treated as an inelastic process in which a molecule is excited by laser radiation to a virtual level and instantly (for 10^{-14} s) emits a photon at a wavelength different from the laser wavelength. The difference of energies of the incident and emitted photons is a characteristic of the scattering molecule and usually corresponds to a change in the vibrational quantum number by unity. Because the Raman scattering cross section is small, the sensitivity of this method is rather limited, which considerably limits its applications. It seems most reasonable to use Raman scattering for remote sensing of waste gases in industrial works, where the concentrations of gas components can be rather high.

When the excitation frequency is close to the allowed transition frequency, the scattering cross section considerably increases (at least, by three orders of magnitude) due to resonance scattering. However, attempts to increase the sensitivity upon such resonance scattering have failed because of the strong absorption of incident and scattered radiation. A distinct feature of this scattering method is that it allows the determination of the ratio of concentrations of any component and a reference gas (for example, nitrogen) from the ratio of Raman signals if the ratio of scattering cross sections is known.

The most promising for atmosphere sensing is the method using Mie scattering. The Mie scattering cross sections can be very high, and even a very small number of scattering particles of size of the order of the laser wavelength can produce a scattering signal that will completely overlap the Rayleigh and Raman signals. Therefore, this method can be used to detect rather low concentrations of dust or aerosol particles. In the case of resonance scattering, the scattering cross section can be very high. However, quenching of excitation in collisions with usual components of the atmosphere, as a rule, strongly reduces the signal, and for this reason this method can be used most efficiently for determining components at low concentrations in the upper atmospheric layers. When molecular fluorescence is used, the collision decay of molecular excitations also reduces the detected signal. A large width typical for molecular fluorescence spectra reduces the signal-to-noise ratio (noise is mainly determined by the background radiation). In this case, an increase in the fluorescence lifetime impairs the spatial resolution.

A single-wavelength lidar, which is the simplest type of lidars, allows one to obtain information on the vertical profiles of the volume extinction coefficient, atmosphere transparency, the upper and lower borders of clouds, etc [1]. However, information obtained with the help of such a lidar is restricted and cannot be used for identification and measuring the parameters of aerosols. Recently numerous attempts have been made to expand the possibilities of lidars by increasing the number of wavelengths for sensing and measuring the depolarisation of scattered signals. A multi-wavelength lidar (aerosol lidar) can be used both for measuring the size distribution of aerosol particles [16] and the refractive index of aerosols [17].

The measurement of elastic depolarisation expands the possibilities of sensing because this allows one to determine

the shape of aerosols (deviation from sphericity) and, hence, the phase state (solid or liquid) [18]. It is known that depolarisation effects in a monostatic lidar are observed upon backscattering due to the deviation of a particle shape from spherical or due to multiple scattering [19]. However, upon sensing with a bistatic lidar, depolarisation also appears due to the 'glory' effect (depolarisation upon scattering at an angle) [20, 21].

A considerable progress in lidar sensing was achieved by using the method of Raman scattering in which elastic scattering (at the incident wavelength) and inelastic (Raman) scattering by a gas under study were detected. The gas concentration in this method is calculated from the ratio of a signal from the gas under study to the reference signal from the gas with known concentration (usually, atmospheric nitrogen or oxygen). The main advantage of the Raman method is that it allows one to identify gases and, unlike the DA method, to perform absolute measurements. In addition, only one laser with a fixed wavelength is used in the Raman method for detecting many components.

The Raman scattering method is widely used for measuring concentrations of H_2O, CH_4, and CO_2 gases despite its low sensitivity compared to that of the DA method. The former method has a high spatial resolution ($\sim$1 m), it does not require the use of complicated tunable lasers and is employed for temperature measurements in the stratosphere, troposphere, and planetary border layer [22].

The applications of the Raman method can be expanded to measure the content of liquid water in the atmosphere [23] and determine the size of particles in clouds [24]. The knowledge of the percentage of liquid water is extremely important for understanding conditions of the formation of aerosols and clouds, as well as for studying condensation processes under the conditions of urban contaminations.

Among the advantages of the Raman scattering method is the possibility of accurate measurements of the profiles of aerosol extinction and scattering and, hence, the calculation of the lidar ratio [25] determined by the ratio of the volume scattering and absorption coefficients. Due to a large enough frequency shift between the laser and Raman lines, the signal in a Raman lidar can be easily separated by means of standard filters. A considerable disadvantage of this method is a low Raman scattering cross section, i.e. a low sensitivity and a low signal-to-noise ratio at low gas concentrations.

In recent years lidars with a variable field of view attract great attention [26]. These lidars can be used to analyse signals caused by multiple scattering, which in turn allows the measurement of the effective size of particles in clouds [27].

A broad scope of problems can be solved by combining the DA and Raman scattering methods [28 – 32]. The DA method is applied for measuring the concentration of gases [33] and the Raman scattering method – for accurate measurements of the profiles of aerosol scattering and extinction [25], as well as the temperature and humidity along the sensing path with a high spatial resolution [28].

3. Operation principle of a DIAL

As mentioned above, the first DA lidar measurements were performed by Schotland who used the temperature tuning of the ruby laser wavelength to the absorption line of water vapour. The maximum sensing height achieved 4.3 km. The DA method was further developed to measure the concentration profiles of the H_2O, NO, NO_2, SO_2, O_3 gases, etc. In practice, the DA lidar sensing of the atmosphere is performed by two methods.

DA lidar method. An atmospheric aerosol was used as a distributed reflector. In this regime, the remote measurement of the concentration profiles of gas components can be measured with the spatial resolution ΔR, determined mainly by the laser pulse duration τ: $\Delta R = c\tau/2$. The lidar based on this principle is called the range-resolved DIAL. The principle of its operation is shown in Fig. 3a.

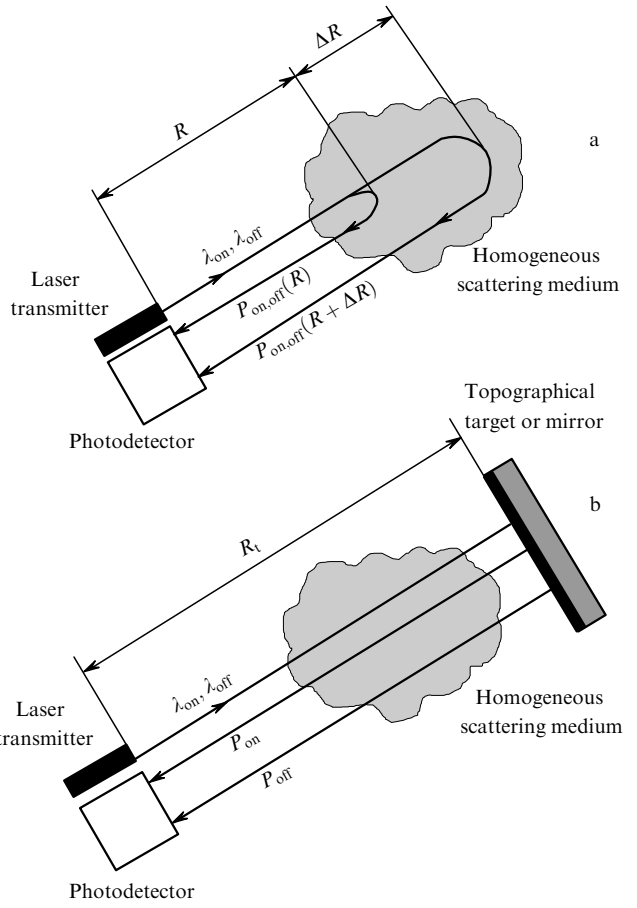

Figure 3. Sensing schemes for lidar (a) and path (b) DA methods (P_{on} and P_{off} are powers of reflected signals at wavelengths λ_{on} and λ_{off}).

DA path method. In this regime, a signal reflected or diffusively reflected from various topographic objects is detected. In this case, it is possible to measure with a high sensitivity the sensing-path-averaged concentrations of gas components along separate directions corresponding to the azimuth of topographic targets. Such a regime is called sometimes the long-path-averaged DIAL method. It is illustrated schematically in Fig. 3b.

The measurement accuracy of gas concentration depends on many parameters:

(i) the detection accuracy of lidar signals (which does not exceed 10 % in real lidar systems [26]);

(ii) the measurement accuracy of the absorption cross section of the gas, which is found either experimentally [34] or from the HITRAN [35] or GEISA spectral data atlases [36];

(iii) optimally chosen pairs of wavelengths inside the absorption line (λ_{on}) and outside it (λ_{off}) [37–39] for which a high differential absorption cross section $\Delta\sigma$ [see below expression (10)], a narrow spectral range $\Delta\lambda = \lambda_{on} - \lambda_{off}$, and the presence of a small number of interfering gases are desirable;

(iv) the measurement accuracy of the aerosol scattering profile;

(v) detector parameters (first of all, its sensitivity).

At present lidars with new algorithms are used where several pairs of wavelengths are employed instead of one [8, 40]. Such an approach strongly reduces the negative influence of an aerosol on the accuracy of concentration measurements by the DA method, especially in the lower part of the troposphere.

Figure 4 presents the absorption spectrum of water vapour [35] at a temperature of 296 K and a pressure of 1 atm. Also, the lines of a CO_2 laser are indicated. One can see that the 10R(20) and 10R(18) lines of a CO_2 laser, whose wavelengths are used as λ_{on} and λ_{off}, are most suitable for the DA sensing of water vapour.

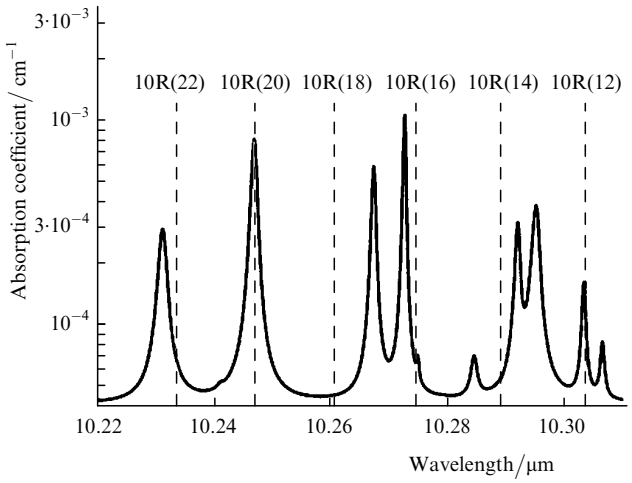

Figure 4. Absorption spectrum of water vapour at 296 K and a pressure of 1 atm in the emission region of a CO_2 laser [35].

Table 1 presents the main pairs of lines of a CO_2 laser used in practice for water vapour sensing and the corresponding differential absorption coefficients [41]. Figure 5 shows the typical lidar signals detected at two of the indicated pairs of lines [41]. Note that these signals were obtained by averaging over 3000–5000 laser pulses. One can see from Fig. 5 that the 10R(12) and 10R(18) lines are suitable for water vapour sensing at ranges up to 10 km, and the 10R(20) and 10R(18) lines – up to 5 km.

Table 1. Main pairs of the lines of a CO_2 laser used for sensing of water vapour and the corresponding differential absorption coefficients.

Line (λ_{on})	Line (λ_{off})	Differential absorption coefficient /atm^{-1} cm^{-1}
10R(20)	10R(18)	8.2×10^{-4}
9R(14)	9R(18)	3.0×10^{-5}
9R(14)	9R(12)	2.1×10^{-4}
10R(12)	10R(10)	2.6×10^{-4}
10R(12)	10R(18)	1.5×10^{-4}

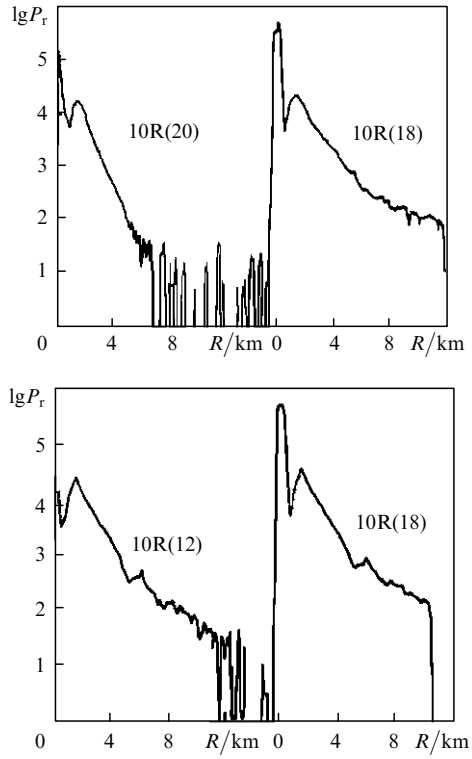

Figure 5. Lidar signals at the lines of a CO_2 laser averaged over 3000–5000 laser pulses [41] (P_r is the received signal power in relative units).

3.1 Basic equations

3.1.1. Lidar equation

The lidar equation in the single elastic scattering approximation is described by the expression [1–3]

$$P_\lambda(R) = P_0 \eta \left(\frac{c\tau}{2}\right) A(R) \frac{\beta_\lambda(R)}{z^2} \exp\left[-2\int_0^R \alpha_\lambda(x)\mathrm{d}x\right], \qquad (1)$$

where R is the distance to the scattering object; c is speed of light; τ is the laser pulse duration; P_λ is the scattered radiation power obtained for the time $t = 2R/c$; P_0 is the laser power; η is the efficiency of the receiver; λ is the laser wavelength; β_λ is the volume backscattering coefficient of the atmosphere; A is the effective area of a detector; and α_λ is the volume extinction coefficient of the atmosphere. The coefficient α_λ can be represented as a sum of terms describing molecular (α_λ^{mol}) and aerosol (α_λ^{aer}) extinction. Note that the molecular extinction coefficient includes absorption $N_g\sigma_g$ in the gas under study, where N_g and σ_g are the gas concentration and absorption cross section, respectively. The scattering coefficient can be also represented as a sum of two terms determining molecular (β_λ^{mol}) and aerosol (β_λ^{aer}) scattering.

One can see from Eqn (1) that to solve it, it is necessary to specify the lidar ratio α/β. The lidar ratio for molecular scattering is $8\pi/3$ sr [1, 2], while for aerosol scattering it depends on many parameters such as the sensing radiation wavelength, the aerosol type, the refractive index of the aerosol medium, and the size distribution function of aerosols [20]. This ratio in the lower troposphere changes from 10 to 110 sr and even to 200 sr [42]. The lidar ratio in a pure atmosphere can be assumed constant, although the error caused by this assumption can be considerable [43].

Usually, the lidar ratio equal to 20 sr is employed, which is typical for scattering by particles of size lower than the wavelength [44].

The molecular scattering ($\beta_\lambda^{\text{mol}}$) and extinction ($\alpha_\lambda^{\text{mol}}$) coefficients can be accurately calculated by using either the Rayleigh scattering theory [19] or a specific model of the atmosphere [45]. According to the Rayleigh scattering theory, the volume molecular backscattering coefficient (in $\text{cm}^{-1}\ \text{sr}^{-1}$) in gases has the form

$$\beta_\lambda^{\text{mol}} = \frac{\pi^2(n^2-1)^2}{N^2\lambda^4}\frac{6+3\Delta}{6-7\Delta}, \tag{2}$$

where N is the molecular concentration; n is the refractive index of the medium; Δ is the degree of depolarisation of scattered radiation. For a mixture of atmospheric gases at heights up to 100 km, the volume backscattering coefficient is described by the expression [2]

$$\beta_\lambda^{\text{mol}} = 5.45\times10^{-28}N\left(\frac{550}{\lambda}\right)^4, \tag{3}$$

where λ is expressed in nanometres.

In the study of single molecular scattering, the parameter Δ is related to the anisotropy of the polarisability of molecules, and in the case of isotropic scattering centres such as monatomic gases of the argon type, it is zero ($\Delta = 0.035$ for air, and 0.036 for nitrogen). The degree of depolarisation during single molecular scattering for main atmospheric gases is presented in Table 2.

Table 2. Degree of depolarisation upon single molecular scattering for main atmospheric gases.

Gas	Δ (%)
Air	3.5
H_2O	2
N_2	3.6
O_2	6.5
CO_2	9.7
SO_2	3.1
H_2S	0.3
CH_4	0
Cl_2	4.1
HCl	0.7
CO	1.3
Ar	0

Note that the emission spectrum broadens somewhat upon molecular scattering (due to the Doppler effect) compared to the emission spectrum of a source. However, this broadening in the Earth atmosphere is relatively small.

The aerosol scattering ($\beta_\lambda^{\text{aer}}$) and extinction ($\beta_\lambda^{\text{aer}}$) coefficients can be determined either from the Mie theory of aerosol scattering [19, 20] or experimentally from lidar signals by using the algorithms for solving the lidar equation. The description of these algorithms is beyond the scope of our paper; the reader can find their description in papers [25, 46–48].

According to the theory of scattering of electromagnetic waves by aerosol particles in the dielectric sphere approximation (the Mie theory) [19], the volume scattering and extinction coefficients at the given wavelength are described by the expressions

$$\alpha^{\text{aer}}(n',\lambda) = \int_0^\infty \pi r^2 Q_{\text{ext}}(\rho,n',\lambda)f(r)\mathrm{d}r, \tag{4}$$

$$\beta^{\text{aer}}(n',\lambda) = \int_0^\infty \pi r^2 Q_{\text{scat}}(\rho,n',\lambda)f(r)\mathrm{d}r, \tag{5}$$

where r is the radius of particles; $f(r)$ is the size distribution function of aerosol particles; n' is the complex refractive index of a dielectric sphere; Q_{scat} and Q_{ext} are the efficiencies of scattering and extinction, respectively; and $\rho = 2\pi r/\lambda$ is the relative size of particles. The aerosol extinction is usually described by the empirical expression [3]

$$\alpha^{\text{aer}} = \frac{3.912}{R_{\text{m}}}\left(\frac{\lambda}{0.55}\right)^{-q}, \tag{6}$$

where R_{m} is the meteorological visibility range at $\lambda = 0.55$ μm. The values of R_{m} for different visibility conditions are presented in Table 3, and the coefficient q is specified as [49]

$$q = \begin{cases} 0.585(R_{\text{m}})^{1/3} & \text{for } R_{\text{m}} \leqslant 6 \text{ km}, \\ 1.3 & \text{for } 6 \text{ km} \leqslant R_{\text{m}} \leqslant 50 \text{ km}, \\ 1.6 & \text{for } R_{\text{m}} \geqslant 50 \text{ km}. \end{cases}$$

Table 3. Meteorological visibility region at a wavelength of 0.55 μm for different meteorological conditions

Visibility conditions	R_{m}/km
Dense fog	< 0.005
Thick fog	0.005–0.050
Usual fog	0.05–0.50
Light fog	0.5–1
Weak fog	1–2
Haze	2–4
Light haze	4–10
Clear	10–20
Very clear	20–30
Perfectly clear	> 50
Pure air	277

The parameter $A(R)$ in Eqn (1) is determined only by the characteristics of a receiver and a transmitter [50]. It depends most strongly on the spatial power distribution in the laser beam and the degree of the overlap of the laser beam and the field of view of a telescope. This factor also takes into account the influence of the shadow of the secondary mirror of the telescope, optical aberration, the inhomogeneity of the detector surface, and the effective area of the telescope. The effective area $A(R)$ of the receiver is described by the expression [2]

$$A(R) = \frac{A_0}{\pi W^2(R)} \times \int_{r=0}^{r_{\max}}\int_{\psi=0}^{2\pi}\xi(R,r,\psi)F(R,r,\psi)r\mathrm{d}r\mathrm{d}\psi = A_0\xi(R), \tag{7}$$

where $F(R,r,\psi)$ is the spatial distribution function of laser radiation; $\xi(R,r,\psi)$ is the geometrical probability coefficient; ψ is the azimuthal angle; $W(R)$ is the laser spot size at the distance R; A_0 is the area of the entrance aperture of the telescope; and $\xi(R)$ is the geometrical factor of the lidar which takes into account the degree of interception of the

laser beam reflected from a target. The geometrical factor of the lidar is called sometimes the function of vignetting caused by the overlap of the receiving and transmitting optical apertures. The latter definition reflects the role of spatial filters in the decrease of the dynamic range of the lidar. The geometrical factor can be either exactly calculated for different lidar configurations [51–54] or determined experimentally [55, 56].

Lidar signals obtained by the DA method are interpreted by using Eqn (1); in the case of the DA path method, the modified equation

$$P_\lambda(R_t) = P_0\eta(\lambda)\frac{A(z)}{R_t^2}\rho_{ins}\exp\left[-2\int_0^{R_t}\alpha_\lambda(x)dx\right] \quad (8)$$

is employed [57], where ρ_{ins} is the instrumental constant which is determined by the reflection coefficient of a topographic target when it is used as a reflector or by the efficiency coefficient of a receiving antennae when a mirror reflector is used; R_t is the distance to the topographic target (Fig. 3b).

3.1.2. Calculation of the gas concentration in the DA method

By using lidar equation (1) for elastic scattering at the wavelengths λ_{on} and λ_{off}, we obtain from the ratio of powers P_{on} and P_{off} of reflected signals at the two wavelengths the expression for the concentration of molecules under study [1, 2]:

$$N(R) = -\frac{1}{2\Delta\sigma}\frac{\partial}{\partial R}\left[\ln\frac{P_{on}(R)}{P_{off}(R)}\right] + \frac{1}{\Delta\sigma}\frac{\partial}{\partial R}\left[\ln\frac{\beta_{on}(R)}{\beta_{off}(R)}\right] - \frac{\alpha_{on}(R)-\alpha_{off}(R)}{\Delta\sigma}, \quad (9)$$

where β_{on} and β_{off} are the backscattering coefficients of the atmosphere at wavelengths λ_{on} and λ_{off}; α_{on} and α_{off} are the extinction coefficients of the atmosphere at λ_{on} and λ_{off};

$$\Delta\sigma = \sigma(\lambda_{on}) - \sigma(\lambda_{off}) = \sigma_{on} - \sigma_{off} \quad (10)$$

is the DA cross section; and $\sigma(\lambda_{on})$ and $\sigma(\lambda_{off})$ are the effective absorption cross sections at the two wavelengths. In the case of the surface sensing path, the cross section for the line centred at ν_0 is well described by the Lorentzian profile [1, 2]

$$\sigma_L(\nu) = \frac{S}{\pi}\frac{\gamma_L}{\gamma_L^2 + (\nu-\nu_0)^2}, \quad (11)$$

where S and γ_L are the intensity and half-width of the absorption line, respectively. The half-width and intensity of vibration–rotation absorption lines at pressure p and temperature T have the form [58, 59]

$$\gamma_L(T,p) = \gamma_L^0\left(\frac{T_0}{T}\right)^l\frac{p}{p_0}, \quad (12)$$

$$S(T) = S_0\left(\frac{T_0}{T}\right)^m\exp\left[-E''\frac{hc}{kT}\left(\frac{1}{T}-\frac{1}{T_0}\right)\right], \quad (13)$$

where γ_L^0 and S_0 are the Lorentzian half-width and intensity at temperature T_0 and pressure p_0; E'' is the energy of the lower vibration–rotation state; h is Planck's constant; k is the Boltzmann constant; and m and l are the parameters of the temperature dependence of the half-width and intensity, respectively. The parameter l for different gases can vary from 0.5 to 1, the parameter m is equal to unity for linear molecules and 1.5 for nonlinear molecules.

Expression (9) shows that the continuous profile $N(R)$ can be reconstructed by recording continuously lidar signals. However, in practice, as a rule, lidar signals are recorded in the form of a discrete digital data base obtained through equal time intervals Δt, which corresponds to the spatial resolution $\Delta R = c\Delta t/2$. Then, from (12) for signals received from atmospheric objects located at distances R and $R+\Delta R$ along the sensing path, the expression is obtained for the average concentration of the gas under study in the indicated interval of distances:

$$\bar{N} = -\frac{1}{2\Delta\sigma\Delta R}\ln\left[\frac{P_{on}(R+\Delta R)}{P_{off}(R+\Delta R)}\frac{P_{off}(R)}{P_{on}(R)}\right] - \frac{\alpha_{on}^{mol}-\alpha_{off}^{mol}}{\Delta\sigma} + B_s + E_a, \quad (14a)$$

$$B_s = \frac{1}{2\Delta\sigma\Delta R}\ln\left[\frac{\beta_{on}(R+\Delta R)}{\beta_{off}(R+\Delta R)}\frac{\beta_{off}(R)}{\beta_{on}(R)}\right], \quad (14b)$$

$$E_a = -\frac{(\alpha_{on}^{aer}-\alpha_{off}^{aer})}{\Delta\sigma}. \quad (14c)$$

The wavelengths are chosen so that the backscattering and extinction coefficient would be independent of the wavelength. Therefore, the spectral interval between the two wavelengths should be small enough to neglect the terms B_s and E_a in (14a). Then, the concentration is described by a simpler expression

$$\bar{N} = -\frac{1}{2\Delta\sigma\Delta R}\ln\left[\frac{P_{on}(R+\Delta R)}{P_{off}(R+\Delta R)}\frac{P_{off}(R)}{P_{on}(R)}\right]. \quad (15)$$

3.1.3. Sensitivity of the DA method

The sensitivity of the DA method is characterised by the minimum concentration N_{min} of the atmospheric gas that can be detected with the minimum measurement error of optical signals in practice. The sensitivity of the DA method was investigated in detail in papers [1–3, 60]. The sensitivity of the DA lidar method can be conveniently estimated from the expression [3]

$$N_{min}(R) = \frac{1}{\Delta\sigma\Delta R}\frac{2}{SNR(R)}, \quad (16)$$

where SNR is the signal-to-noise ratio at the distance R from the lidar.

To increase the sensitivity at the given spatial resolution ΔR, the most intense absorption lines of the gas under study with the maximum DA cross sections $\Delta\sigma$ should be selected. This is admissible only for the long-path DA method. For the DA lidar method, the situation is different because the measurement error of lidar signals considerably changes, as a rule, along the sensing path and, hence, the lidar sensitivity also changes along this path. In this case, the choice of the most intense absorption lines of the gas can reduce the sensitivity in a volume located at the distance R from the lidar.

One can also see from expression (16) that for large signal-to-noise ratios the concentration N_{min} is limited by the systematic error of the lidar, which is typically 10 % – 20 % [61].

The sensitivity of the DA method depends to a great extent on the laser linewidth, decreasing with increasing the latter [1, 2]. In practice, the absorption line should be selected for which the ratio $\Delta\sigma/\Delta\lambda$ is maximal [42], where $\Delta\lambda = \lambda_{on} - \lambda_{off}$.

3.2 Error sources in the DA method

A detailed analysis of the errors of the DA laser sensing of humidity was performed by the founder of this method Schotland [62]. The analysis showed that the main sources of errors are measurement errors, errors in *a priori* calculation of the absorption coefficients and variability of the atmosphere. Schotland considered the idealised case assuming that the laser linewidth was negligibly small. In practice, the instrumental function of the spectral distribution of the laser radiation power considerably affects the results of measurements, and in some cases it is necessary to take into account a number of error sources in lidar measurements. Such errors were taken into account for the first time in papers [63, 64]. Table 4 presents the main error sources of the DA method considered in these papers.

The errors related to the first four sources (Table 4) are caused by the instrumental distortions of lidar signals upon their detection. They are associated both with the parameters of laser radiation and a receiving system. The common feature of these errors is that they can be in principle completely eliminated by selecting properly the parameters of the lidar. The errors related to other sources are caused by the objective influence of the atmosphere itself. This influence can be only partially corrected but not completely eliminated by varying the lidar parameters. Errors of the fourth type concern lidars containing photomultipliers [65]. Errors related to the sixth and seventh sources can achieve 16 % and 26 %, respectively.

Table 4. Main error sources of the DA method.

Instrumental	Atmospheric
1. Finite laser linewidth	5. Variation in scattering properties of the atmosphere
2. Instability of the laser wavelength	6. Doppler broadening
3. Noise in the laser spectrum	7. Absorption line shift
4. Nonlinear distortions in a photodetector	8. Temperature variations
	9. Pure rotational Raman signals
	10. Absorption by various interfering gases

All the possible measurement errors are described in detail in papers [62, 66 – 70] and the methods of their reduction – in papers [71 – 73]. Note only that the measurement accuracy of the gas concentration when the laser linewidth is equal to the absorption linewidth of a gas can exceed 40 %. The instability in the laser frequency can cause the measurement error up to 30 % during land-based lidar sensing.

The classical formula for the measurement error of the average concentration of a gas in the interval ΔR has the form [42]

$$\delta\bar{N} = \frac{1}{2\Delta\sigma\Delta R}\left[\frac{2}{N_p}(\delta_{on}^2 + \delta_{off}^2) + \delta_s^2\right]^{1/2}, \quad (17)$$

where N_p is the number of pulses in a series used to obtain the given result; δ_{on} and δ_{off} are random errors in the detection of signals at the wavelengths λ_{on} and λ_{off}; δ_s is the systematic error that is not related to the detector noise. The values of δ_{on} and δ_{off} are usually calculated in terms of the signal-to-noise ratio.

The systematic error is determined by terms B_s (14b) and E_a (14c). It is described by the expression [74]

$$\delta_s^2 = 2(\delta_{\beta^{aer}}^2 + \delta_{\beta^{mol}}^2)\left(\frac{\beta_{off}^{aer}\beta_{on}^{mol} - \beta_{on}^{aer}\beta_{off}^{mol}}{\beta_{off}\beta_{on}}\right)$$
$$+ (2\Delta R)^2[(\alpha_{on}^{aer} - \alpha_{off}^{aer})^2\delta_{\alpha^{aer}}^2 + (\alpha_{on}^{mol} - \alpha_{off}^{mol})^2\delta_{\alpha^{mol}}^2]$$
$$+ (2\Delta R)^2\sum_{j=1}^{M}[\Delta\sigma_j^2\delta_{N_j}^2 + \delta_{\Delta\sigma_j}^2 N_j^2] + (2\Delta\sigma\Delta R)^2\delta_{\Delta\sigma}^2, \quad (18)$$

where $\delta_{\beta^{aer}}$ and $\delta_{\beta^{mol}}$ are the relative measurement errors of the backscattering coefficients for aerosol particles and molecules in the atmosphere, respectively; $\delta_{\alpha^{aer}}$ and $\delta_{\alpha^{mol}}$ are relative errors caused by absorption of laser radiation by aerosol particles and molecules in the atmosphere, respectively; δ_{N_j} and $\delta_{\Delta\sigma_j}$ are the specification or measurement errors of the concentration of the jth interfering gas and its differential absorption cross section, respectively; N_j and $\Delta\sigma_j$ are the concentration and differential absorption cross section of the jth interfering gas, respectively; and $\delta_{\Delta\sigma}$ is the specification or measurement error of the differential absorption cross section of a gas under study.

The first two terms in (18) are related to the dependence of the scattering properties of a medium upon the laser wavelength tuning. These terms should be taken into account upon sensing ozone in the UV region. The third term should be taken into account in the presence of interfering gases. When isolated absorption lines are used, the first three terms can be omitted. The last term is related to the measurement error of the gas absorption cross section.

3.3 Field of applications of the DA method

The DA lidars have wide applications and can be classified according to different properties such as the spectral range [the near-IR (between 0.7 and 2.5 μm) and mid-IR (from 2.5 to 14 μm) regions], the sensing range, the lidar system basing (mobile, stationary, spaceborne or airborne), the sensing region (troposphere or stratosphere), parameters being sensed: metrological parameters at the global or local scale (pressure and temperature profiles) and concentrations of various pollutants in the atmosphere (CH_4, HCl, NH_3, SF_6, C_6H_6, O_3, C_2H_4, N_2H_4, CO, N_2O, CO_2, HNO_3, OSC, CS_2, Freons, dioxins, organic gases, hydrazine, rocket fuels, and war toxic gases).

Humidity can be determined by the DA method by using a proper absorption band of water. For example, the 10R(20) and 10R(18) absorption lines of water vapour located in the emission region of a CO_2 laser can be used as λ_{on} and λ_{off} (Fig. 2). In airborne lidar systems, the 940-nm and 716.98-nm absorption bands in the near-IR region overlapping with the lines of the alexandrite and Ti : sapphire lasers are commonly used [75]. The DA

measurements of pressure and temperature are based on the dependence of the absorption cross section of atmospheric oxygen on pressure and temperature, as follows from expressions (12) and (13). The parameter l in expression (12) is 0.7 for oxygen and 0.62 for water vapour [35]. The Doppler width of the 766-nm absorption line of oxygen at 273 K is 0.0136 cm^{-1}, i.e. it is comparable with the Lorentzian width in air at the atmospheric pressure (0.035 – 0.06 cm^{-1}) [2]. This wavelength (an alexandrite laser) is used for DA measurements of the temperature and pressure of the atmosphere. It was shown in [75] that humidity can be determined by the DA method in the height range from 0 to 1.8 km with an error of no more than 10 % and temperature in the height range from 0 to 1.2 km with an error of no more than 0.5 K.

4. Types of IR lidars

It was shown in [76] that the IR region is more suitable than the UV region for spaceborne DA lidar sensing of ozone in the lower troposphere. The IR region, especially in the range from 2.5 to 14 μm, is very promising for atmosphere sensing because the intense absorption lines of almost all atmospheric gases lie in this region (Fig. 6). In addition, six transparency windows of the atmosphere are located in the IR region (Fig. 7): 0.95 – 1.06 μm, 1.2 – 1.3 μm, 1.5 – 1.8 μm, 2.1 – 2.4 μm, 3.3 – 4 μm, and 8 – 14 μm. Note that the transmission spectrum of the atmosphere shown in Fig. 7 is recorded with a low spectral resolution. This spectrum recorded with a high resolution reveals many microwindows within each of the above windows. It is these microwindows that are of interest for lidar sensing. To measure the energy losses of laser radiation due to absorption by atmospheric gases and aerosol particles, it is necessary to know the emission spectrum of the laser and absorption spectra of gases and aerosols. The laser wavelengths lying within the transparency window of the atmosphere are the most promising for atmosphere sensing.

Table 5 presents the wavelengths of the main IR lasers of interest for lidar sensing of the atmosphere. In the mid-IR region, the DF, CO_2, and NH_3 lasers are used, as a rule. The emission lines of these lasers are optimal for long-range sensing of the atmosphere. For the near-IR sensing, the solid-state ruby ($Cr : Al_2O_3$), Ti : sapphire ($Ti : Al_2O_3$) and alexandrite ($Cr : BeAl_2O_4$) lasers are optimal candidates. However, they can be used for sensing of only few gases because the tuning range of these lasers is comparatively narrow. For this reason, optical parametric oscillators

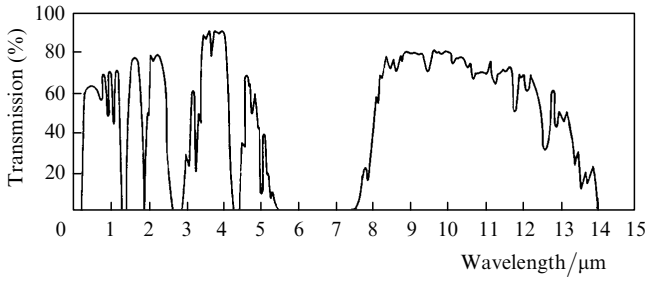

Figure 7. Transmission in the atmosphere in the horizontal path of length 1882 m at the sea level [2].

Table 5. Wavelengths of main IR lasers used for lidar sensing of the atmosphere.

Laser	λ/μm
Ruby ($Cr : Al_2O_3$)	0.6943
Alexandrite ($Cr : BeAl_2O_4$)	0.74 – 0.78
Ti : sapphire ($Ti : Al_2O_3$)	0.7 – 1.1
Nd : YAG	1.064
Nd : YLF	1.053
Er : YAG	2.94
Er : YLF	1.73
Ho : YLF	2.04
He – Ne	0.63; 1.15; 3.39
DF	3.6 – 4.1
CO (first overtone)	5 – 7 (2.5 – 4.2)
CO_2	9 – 11
NH_3	11 – 13.5
GaAs	0.84
$GaAs_{1-x}P_x$	0.64 – 0.84
$InAs_{1-x}P_x$	0.9 – 3
$Pb_{1-x}Sn_xSe$	8 – 34

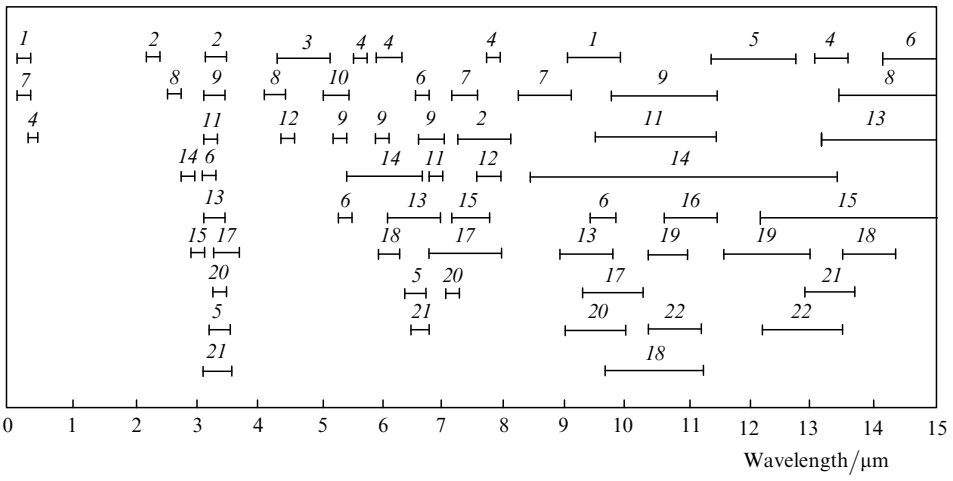

Figure 6. Positions of the absorption bands of some gases in the spectral range from 0.25 to 15 μm [2]: O_3 (*1*), CH_4 (*2*), CO (*3*), NO_2 (*4*), C_2H_6 (*5*), C_6H_6 (*6*), SO_2 (*7*), CO_2 (*8*), C_3H_6 (*9*), NO (*10*), C_2H_4 (*11*), N_2O (*12*), C_7H_8 (*13*), NH_3 (*14*), C_2H_5 (*15*), C_4H_6 (*16*), CH_3OH (*17*), C_2H_3Cl (*18*), C_2HCl_3 (*19*), C_2H_5OH (*20*), C_3H_8 (*21*), C_2Cl_4 (*22*).

(OPOs), second-harmonic and third-harmonic generators are usually employed in the near-IR region. Also, frequency converters based on Raman scattering in H_2, D_2, and CH_4 are used, in which the frequency shift is 4155, 2986, and 2917 cm^{-1}, respectively. This method is the simplest and economical and it was successfully employed to obtain lasing at 720 and 940 nm upon pumping by a dye laser and also lasing at 940 nm upon pumping by a Nd : glass laser [2, 3].

To cover the near-IR region, OPOs are often used. For example, a CdSe OPO pumped by a 2.96-μm Er : YAG laser and a 2.36-μm Dy : CaF_2 laser provides continuous tuning in the spectral regions 2.8 – 4.2 μm and 7.5 – 13.7 μm, respectively. The near-IR region can be also covered by using CO_2 and CO lasers for second- and third-harmonic generation in nonlinear $CdGeAs_2$ and $ZnGeP_2$ crystals [7].

Recently spin-flop Raman lasers have gained widespread acceptance. The emission of these lasers covers the spectral range from 1.7 to 13 μm upon pumping by a CO_2 laser and 5 – 6 μm upon pumping by a CO laser [77].

Among the existing tunable lasers (Table 5), only semiconductor lasers cover the entire IR region; however, their low output power hinders their application in lidars [78]. Nevertheless, semiconductor lasers can be used indirectly for sensing of the atmosphere as pump sources for solid-state lasers. The pumping of a Nd : YAG laser by a GaAs laser at 808 nm results in the increase in the output power by an order of magnitude compared to traditional pumping [77].

Note that molecular scattering in the IR region above 1 μm is negligible compared to aerosol scattering. One can see from expressions (2) and (6) that the molecular scattering coefficient is proportional to λ^{-4}, while the aerosol extinction coefficient is proportional to λ^{-q}, where q is a constant varying from 1.2 to 2.5 depending on the size distribution of aerosols, their shape, and refractive index [79].

In the IR DA lidar sensing, the systematic error related to a finite laser linewidth should be taken into account. The estimates presented in [80] show that accurate measurements by this method in the troposphere at the laser wavelength ~ 10 μm can be provided if the laser linewidth is ~ 100 MHz. At the same time, accurate sensing in the stratosphere requires even a smaller laser linewidth (~ 10 MHz).

The detector type is determined by the spectral region of observations, which in turn depends on the spectral range of the laser used. In the UV, visible, and near-IR ($\lambda < 1.1$ μm) lidars, photomultipliers are successfully used for detecting reflected signals. In the mid-IR region, only thermal and photoelectric semiconductor detectors can be used. Figure 8 presents the spectral curves of the main types of detectors (photodiodes and photoresistors) used in IR lidars [2]. At present nitrogen-cooled and sometimes uncooled photodetectors based on triple $Hg_xCd_{1-x}Te$ [cadmium – mercury – tellurium (CMT)] semiconductor compounds are used in IR lidars [81, 82].

The problem of a low sensitivity of mid-IR detectors is solved, as a rule, by using heterodyne detection [3, 83, 84]. The operation range of direct-detection mid-IR lidars, for example CO_2 lidars, is 2 – 3 km. With the heterodyne detection, the sensing range achieves 10 km for the same parameters of the lidar. However, this advantage is lost due to a lower sensitivity compared to direct-detection lidars due to the influence the speckle noise [85].

4.1 Near-IR lidars

The first lidar system based on a solid-state (ruby) laser was fabricated in the mid-1960s for the DA sensing of water vapour. A low pulse repetition rate and the instability of the ruby laser wavelength resulted in large measurement errors. In the next generation of solid-state lasers, an alexandrite laser emitting in the region between 0.74 and 0.78 μm was used. The absorption bands of water vapour suitable for DA sensing in the lower troposphere and for temperature and pressure measurements fall within this spectral range. Recently a Ti : sapphire laser has received wide applications. The wavelength of this laser can be continuously tuned between 0.7 and 1.1 μm and its

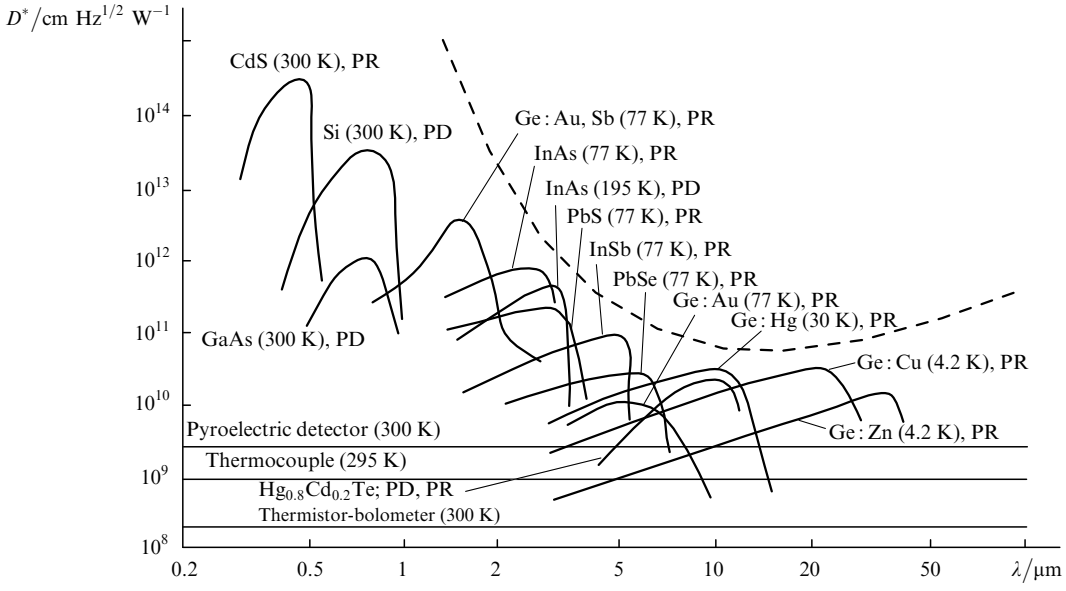

Figure 8. Spectral curves of the detection ability D^* of various photoresistors (PR) and photodiodes (PD) [2]. The dashed curve corresponds to the ideal photodetector limited by the shot noise of a background radiation source (the field of view angle is 180°, the background temperature is 300 K).

maximum output power is achieved at 0.8 μm. The absorption bands of water vapour at ~940 nm, which can be used for its sensing in the upper troposphere, the lower stratosphere and in a very dry atmosphere, fall within this spectral range.

The near- and mid-IR regions can be covered by radiation from OPOs based on nonlinear crystals. Table 6 presents the main nonlinear crystals used in OPOs and for SHG and THG [86]. Classical OPOs pumped by a Nd : YAG laser are usually based on KTP, KDP, $LiNbO_3$, LBO, and BBO crystals; therefore, the long-wavelength boundary of their radiation does not exceed 5 μm. The CdSe OPOs pumped by a 2.96-μm Er : YAG laser and a 2.36-μm Dy : CaF_2 laser are continuously tunable in the ranges from 2.8 to 4.2 μm and from 7.5 to 13.7 μm, respectively.

Table 6. Main nonlinear crystals used in OPOs and for SHG and THG.

Crystal	Transmission region/μm
ADP	0.18 – 1.5
KDP	0.18 – 1.7
CDA	0.27 – 1.7
$LiNbO_3$	0.33 – 5.5
BBO	0.20 – 2.2
KTP	0.35 – 4.5
LBO	0.16 – 2.3
$AgGaS_2$	0.50 – 13
$AgGaSe_2$	0.71 – 18
CdSe	0.75 – 20
$ZnGeP_2$	0.74 – 12
Tl_3AsSe_3	1.30 – 13

In [87], a CdSe OPO pumped by a 2.96-μm Er : YAG laser was used for sensing of NH_3, CH_4, CO, and HCl. The main parameters of this OPO are presented below. This lidar operates in the DA path regime and provides the detection of these gases at the maximum permissible concentration (MPC) level over distances from 0.1 to 1 km.

CdSe crystal length/mm 40
Lasing region/μm . . . . . 2.8 – 4.2
Laser linewidth/cm^{-1} 1
Lasing efficiency (%) . . . . . 1 – 10
Pulse duration/ns . . . . . 30 – 40
Pulse energy/mJ . . . . . 3 – 4
Pulse repetition rate/Hz 10

One of the most efficient methods for obtaining new wavelengths suitable for IR sensing of the atmosphere is the second and third harmonic generation. Second-harmonic radiation in a $ZnGeP_2$ crystal pumped by a CO_2 laser covers the spectral range between 4.5 and 5.5 μm with the frequency conversion efficiency 10 % – 20 %. The sensitivity of InSb detectors in this spectral range is five times higher than that of CMT detectors used in a CO_2 lidar (9 – 11 μm). Third-harmonic radiation in the same crystal pumped by the same laser covers the spectral range from 3 to 3.7 μm. The sensitivity of InAs detectors in this spectral range is five times higher than that of InSb detectors. Note also that the emission spectrum of a CO_2 laser and its harmonics fall within the atmospheric transparency window. SHG and THG in a $CdGeAs_2$ crystal pumped by a CO_2 laser are used in lidars abroad. Note that a $CdGeAs_2$ crystal has the same parameters as a $ZnGeP_2$ crystal, but requires cooling.

In [7], a lidar system is described in which SHG in a $ZnGeP_2$ crystal pumped by a CO_2 laser is used for remote sensing of carbon monoxide CO and OSC. The absorption coefficient of carbon monoxide at the second-harmonic wavelength of the 9R(18) line of a CO_2 laser is 29.7 atm^{-1} cm^{-1}.

The radiation of a Co : MgF_2 OPO pumped by a 1.064-μm Nd : YAG laser can be continuously tuned in the range from 1.5 to 2.3 μm. This OPO was used in [88] for sensing of HCl, CH_4, and H_2O. The sensing wavelengths and absorption coefficients of each of these gases are presented in Table 7. The sensing range of this system, whose parameters are presented below, can achieve 6 km in the DA path regime and 3 km in the DA lidar regime. The first tests of this system showed that it provides the sensing sensitivity for HCl and CH_4 down to 1 and 10 ppb, respectively, at distances up to 3 km.

Table 7. Parameters of the absorption lines of detected gases used in [88].

Gas	λ/μm	Absorption coefficient/atm^{-1} cm^{-1}
HCl	1.7525	0.43
CH_4	1.6713	0.036
H_2O	1.7515	8.3×10^{-3}

Co : MgF_2 OPO
Pulse energy/mJ 10
Pulse duration/ns 300
Cassegrain telescope
Diameter/cm 30
Focal distance/cm 100
Cooled InSb detector
Diameter/mm 2
Detection ability/cm $Hz^{1/2}W^{-1}$ . . . . . 10^{11}

A microsecond laser system described in [89] has unique parameters: a small size, a high pulse repetition rate (500 Hz), and the lidar operation range up to 5 km. This system uses an OPO pumped by a Yb : YAG laser and covers the spectral range from 3 to 5 μm. It is intended for sensing of toxins with good accuracy (10 %) and high sensitivity (10 ppb). The size of the system was diminished by using a Cassegrain telescope of diameter 35 cm.

In [90], a unique system is described in which an OPO based on a BBO crystal pumped by a Nd : YAG laser is used. The system is intended for simultaneous sensing of several atmospheric parameters (backscattering coefficients at 555 and 829 nm, temperature, atmospheric transmission, contents of water vapour and contaminants). The OPO in this system operates with a pulse repetition rate of 100 Hz and can be continuously tuned in the spectral range from 0.4 to 2.5 μm. The receiving part of this lidar consists of two identical Newton telescopes with the objective diameters 30 cm. The first telescope is used when the lidar operates by the DA method, and the second one is used in the Raman method ($\lambda = 1064$, 532, 407, 386, and 355 nm). This system can be used for sensing of the atmosphere up to a height of 2 km with a spatial resolution of 3 m. However, after smoothing of signals, the spatial resolution is impaired to 30 m. Tests of this system under urban conditions showed that the aerosol backscattering coefficient was maximal at a

height of 100 m, being 6×10^{-8} cm^{-1} sr^{-1} at 355 nm and 3×10^{-8} cm^{-1} sr^{-1} at 826 nm.

The lidar system described in [91] uses a $LiNbO_3$ OPO pumped by a Nd : YAG laser. The emission spectrum of this OPO in the range from 3 to 3.5 μm permits the sensing of methane and propane, but the output energy of this lidar restricts the sensing range of these gases by 0.5 km at the spatial resolution $\Delta R = 30$ m and a sensitivity of 0.1 ppm for methane and 0.4 ppm for propane,

In [92–94], airborne lidars for sensing of hydrocarbon molecules are described. All the lidars use $LiNbO_3$ OPOs which can be continuously tuned in the spectral range from 2 to 5 μm. Due to a low output energy of OPOs, the DA path method is employed in these lidars.

In [95], the lidar system for sensing of methane and propane over a range of 1 km and aerosols over a range of 8 km was studied. The system uses a Nd : YAG laser-pumped OPO emitting in the range from 1.45 to 4 μm employed for sensing of methane and propane and a 1.536-μm erbium glass laser for sensing of aerosols. The mobile lidar system described in [96] is intended for long-range sensing of propane and methane and operates in the DA path regime, although it does not differ considerably from the system studied in [95].

4.2 Mid-IR lidars

The intense absorption bands of many gases contaminating the atmosphere fall within the mid-IR range between 2.5 and 14 μm [35, 36, 97]. At the same time, the emission spectra of high-power and efficient lasers such as NH_3, CO_2, CO, and DF lasers cover this range and their lines fall within the atmospheric transparency windows between 3 and 5 μm and 8 and 14 μm. Therefore, the mid-IR region is quite promising for the remote lidar ecological monitoring of the atmosphere.

4.2.1. He–Ne lidar

The leakage of methane is detected by using the 3.3913-μm and 3.3903-μm lines of a He–Ne laser which fall within the absorption band of methane (Fig. 9). The simplicity and availability of a He–Ne laser employed for solving this important problem is the main advantage of the system proposed in [98]. The technical parameters of the lidar are presented below. The output power of the laser used in the lidar is relatively low (2 mW), which is typical for lasers of this type. However, the lidar detects methane with a rather high sensitivity (3 ppb m) because a reflector (topographical target) is used. This lidar can detect many natural gases whose absorption cross sections are presented in Table 8.

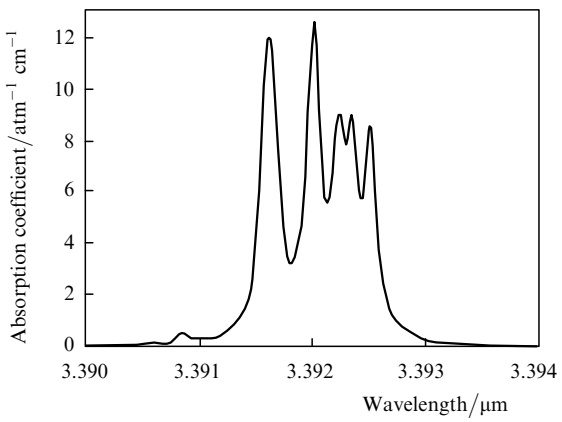

Figure 9. Absorption spectrum of methane in the emission region of a He–Ne laser [35].

He–Ne laser

Power/mW	2
Divergence/mrad	5

Mechanical chopper

Pulse repetition rate/kHz	2
Aperture/mm	5
Phase difference/deg	90

Receiving optics/mirror

Diameter/cm	37
Focal distance/cm	88

InSb detector

Diameter/mm	2
Detection ability/cm Hz$^{1/2}$ W^{-1}	10^{11}

Optical filter

Transmission bandwidth (%)	4.2
Maximum transmission (%)	70
Temperature/K	77

Table 8. Main gases detected in paper [98] and the corresponding differential absorption coefficients for the used wavelengths λ_{on} and λ_{off}.

Gas	Differential absorption coefficient/atm^{-1} cm^{-1}
Methane	7.7 ± 0.2
Ethane	2.2 ± 1.2
Propane	0.9 ± 0.1
n-butane	0.2 ± 0.6
iso-butane	1.9 ± 0.4

4.2.2. DF lidars

The DF laser emits in the spectral range from 3.5 to 4.1 μm, and its emission spectrum falls within one of the atmospheric transparency windows. For this reason, this laser was used in lidars in [91, 99, 100].

Table 9 presents the sensing parameters of three substances obtained by means of a DF lidar [99]. The main

Table 9. Main gases detected in paper [99], the corresponding differential absorption coefficients for the used wavelengths λ_{on} and λ_{off}, and detection sensitivities.

Molecule	Differential absorption coefficient/atm^{-1} cm^{-1}	Sensitivity/ppb km
HCl	5.64	0.05
CH_4	0.047	6
N_2O	1.19	0.24

DF laser

Pulse energy/mJ	150–200
Pulse duration/μs	1.0
Pulse repetition rate/Hz	1/6

Newton telescope

Diameter/cm	31.75
Field of view/mrad	3.0

CMT detector

Detection ability/cm Hz$^{1/2}$ W^{-1}	5×10^9
Receiving area size/mm	1×1
Time constant/ns	75

technical parameters of the DF laser used in [99] are listed on the previous page.

In [91], the results of first tests of the lidar system based on a high-power DF laser are presented. The parameters of this laser are listed below. The system is intended for the long-range identification of aerosols by using resonance scattering. The first tests showed that the system can be used for sensing a tributinamine cloud of width 100 m with concentration 2–3 mg m^{-3} over distances up to 15 km.

Pulse energy/J 150
Pulse duration/μs 2
Divergence/mrad 0.1
Emission region/μm . . . . . 3.6–4.1 (> 30 lines)
Maximum single-line energy/J 8
Minimum separation between pulses/min 5
Operation readiness time/s 10

The presence of interfering gases such as water vapour and HDO strongly affect the accuracy of DA DF lidar measurements and the sensing range (no more than 2–3 km) despite a rather high pulse energy.

4.2.3. CO_2 lidars

At present the most convenient for applications in lidars is a CO_2 laser emitting in the spectral region from 9 to 11 μm which falls within the 8–14-μm atmospheric transparency window. Due to their simplicity and reliability, high energy parameters of the smooth and quasi-distant emission spectrum, as well as high operation characteristics, these lasers are series-produced, being permanently modernised. In addition, the absorption lines of more than 90 gases such as NH_3, C_2H_2, H_2O, O_3, CO_2, N_2O, NO_2, HNO_3, SF_6, OSC, CS_2, Freons, organic gases, hydrazine, components of rocket fuels, and war toxic gases fall within the tuning range of a CO_2 laser [7, 97]. Figure 10 presents the emission spectrum of a CO_2 laser [85]. The spectrum consists of more than 60 lines, covering discretely the spectral range from 9 to 11 μm.

The CO_2 lidars were thoroughly studied and optimised by various research groups [66, 69, 71, 84, 101–122]. At present different types of CO_2 lidars are used for environment sensing [83, 98, 104, 123–134].

Table 10 presents substances sensed with a CO_2 lidar, their differential absorption coefficients, and the DA lidar sensitivities for each of the substances [99]. One can see that the sensitivity of the CO_2 lidar for some substances (NH_3, SF_6, CCl_2F_2) is very high, whereas for CO_2 this lidar cannot be applied at all. The sensitivity $\sim 10^4$ ppb for the water vapour sensing is considered normal because the concentration of H_2O in the atmosphere is high enough. SF_6 is a typical gas detected by the CO_2 lidar. One can see from the absorption spectrum of SF_6 presented in Fig. 11 [35] that absorption in the emission region of the CO_2 laser is rather high.

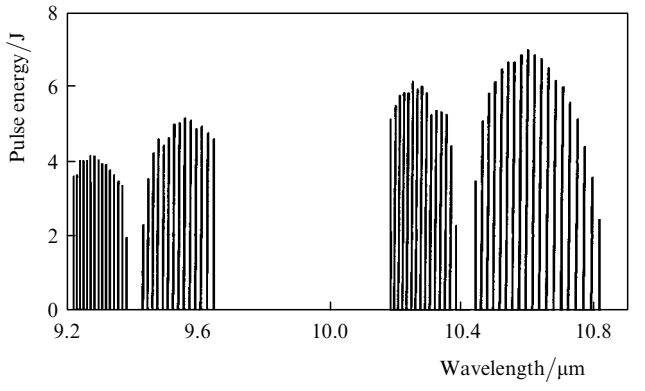

Figure 10. Emission spectrum of the TEA CO_2 laser [85].

Table 10. Substances detected with a CO_2 lidar, the corresponding absorption coefficients and detection sensitivity [99].

Molecule	Differential absorption coefficient/atm^{-1} cm^{-1}	Sensitivity/ppb km
NH_3	120	0.42
C_6H_6	2.3	22
1.3-butadeine	2.45	15
CO_2	1.8×10^{-3}	28000
C_2H_4	33.0	1.5
$C_2Cl_3F_3$	19.2	2.6
CCl_3F	31.0	1.6
CCl_2F_2	92.0	0.55
CH_3OH	19.4	2.6
O_3	12.7	4.0
C_2Cl_4	28.5	1.8
SO_2	6.73	7.5
SF_6	800.0	0.063
C_2HCl_3	14.0	3.6
C_2H_3Cl	6.79	7.4
H_2O	8.36×10^{-4}	60000

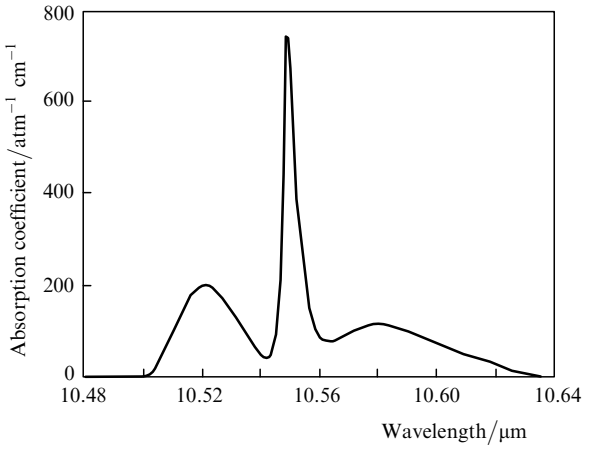

Figure 11. Absorption spectrum of SF_6 in the emission region of the CO_2 laser [35].

In [123], an airborne lidar agent remote monitor (ALARM) for sensing of SF_6 is described. The absorption coefficients of this gas at the emission wavelengths of the CO_2 laser are presented in Table 11. This monitor uses two TEA CO_2 lasers emitting 1.5-J pulses at the 10P(20) line and a telescope with the primary mirror of diameter 35 cm.

Figure 12 shows the scheme of the unique TEA CO_2 lidar developed at the Institute of Atmospheric Optics, Siberian Branch, RAS and Tomsk State University [124–126]. The lidar is intended for control of the gas composition of the atmosphere under field conditions and is a prototype of a commercial field remote gas analyser. The lidar can operate in the path and lidar DA regimes.

Table 11. Absorption coefficients of the SF_6 gas at the lines of a CO_2 laser [35].

CO_2 laser line	λ/μm	Absorption coefficient/ atm^{-1} cm^{-1}
10P(32)	10.71857	20
10P(30)	10.69639	9
10P(28)	10.67459	28
10P(26)	10.65316	70
10P(24)	10.6321	130
10P(22)	10.61139	200
10P(20)	10.59104	330
10P(18)	10.57105	430
10P(16)	10.55139	800
10P(14)	10.53209	290
10P(12)	10.51312	350
10P(10)	10.49449	18

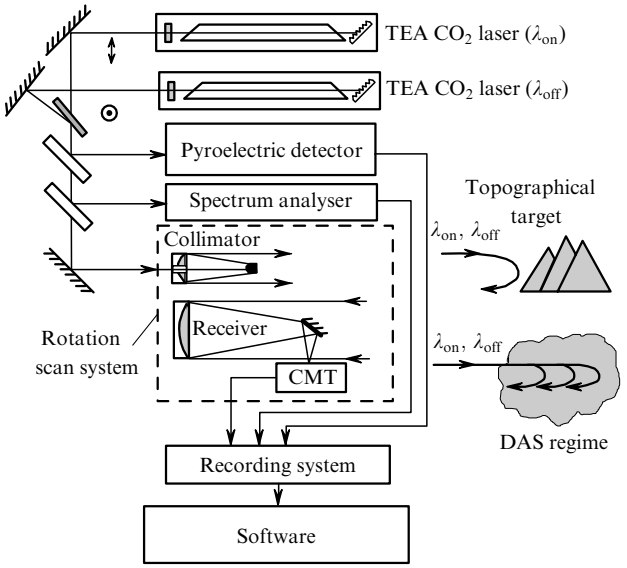

Figure 12. Scheme of the differential-absorption and scattering (DAS) CO_2 lidar [102].

The main feature of this lidar is the possibility to control all its parameters: the distance between the axes of the receiving and transmission telescopes, the divergence angle of their axes, and the size of field apertures and (or) the sensitivity of a photomultiplier. The sensing radiation at the collimator exit is focused at a distance up to 3 km. The TEA CO_2 laser used in this lidar emits 1–8.8-J, 30-ns pulses with a pulse repetition rate of 2 Hz. The emission spectrum of this laser consists of 85 lines in the spectral range from 9.15 to 10.86 μm. The weight of the laser head of size $1300 \times 300 \times 350$ cm is 70 kg. The lidar shown schematically in Fig. 12 was used to measure the concentration of NH_3, HCl, CO, and CH_4 at the MPC level in the path regime over paths of lengths from 0.1 to 1.0 km.

In the scheme in Fig. 12, two lasers are used to realise the DA method. One of them generates a pulse at the wavelength λ_{on} coinciding with the centre of the absorption line of a gas, while another generates simultaneously a pulse at the wavelength λ_{off} lying in the wing of the absorption line. The delay between the two pulses should not exceed 1 ms [66] in order to assume that the atmosphere is frozen.

To realise the DA method more economically, the scheme of a two-frequency CO_2 radiation source with

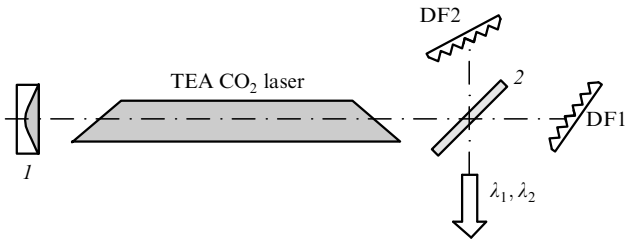

Figure 13. Optical scheme of a two-frequency CO_2 laser with self-combined beams [135]: (*1*) highly reflecting mirror; (*2*) beamsplitter; DF1 and DF2 are diffraction gratings tuned to the wavelengths λ_1 and λ_2.

the self-combined laser beams was proposed [135] (Fig. 13). The idea is to obtain laser radiation at two wavelengths λ_{on} and λ_{off} with the help of a Michelson interferometer and two diffraction gratings and realise the DA method by maintaining the condition of the 'frozen' atmosphere.

The first experiments showed that such a CO_2 laser scheme provides simultaneous lasing at two wavelengths λ_1 and λ_2 if $\Delta\lambda = \lambda_1 - \lambda_2 > 50\ cm^{-1}$. If the frequencies to which the gratings are tunes are close, the light beam consists of one spectral component at an intermediate frequency. Note that similar optical scheme can be also used with other lasers.

The sensing range of CO_2 lidars in the direct detection regime is usually 2–3 km because of a low sensitivity of detectors in this region (Fig. 8) and a low aerosol scattering coefficient [101, 102]. The sensing range is usually increased by employing heterodyne detection [84]. In [110], the MAPM (mobile atmospheric pollutant mapping) lidar based on a TEA CO_2 laser with heterodyne detection is described. This lidar is intended first of all for long-range sensing of water vapour [41] and environmental pollutants. Figure 14 shows the functional scheme of this lidar in which two single-mode TEA CO_2 lasers are used. The lidar can operate in the direct detection regime (the sensing range is 1–3 km) and in the heterodyne detection regime (5–10 km) with a spatial resolution of 30 m. The main technical parameters of the MAPM lidar are presented below.

Transmitting system consisting of two TEA CO_2 lasers

Pulse energy/mJ 60
Pulse repetition rate/Hz 50–150
Pulse duration/μs 0.5–2
Operating wavelengths/μm 9.2–10.7
Lasing regime . . . . . single-mode

Receiving system

Nonaxial parabolic telescope

Diameter/m 0.3
Focal distance/m 1.5

CMT detector cooled to 77 K

Receiving area size/mm . . . . . 0.25×0.25

ADC

Passband/MHz 5
Binary digit/bit 10

In [128], the unique ADEDIS (appareil de detection à distance) direct-detection lidar is described which is based on a high-power TEA CO_2 laser emitting 1.2-J pulses at the 10P(20) line with a pulse repetition rate of 10 Hz. The tests

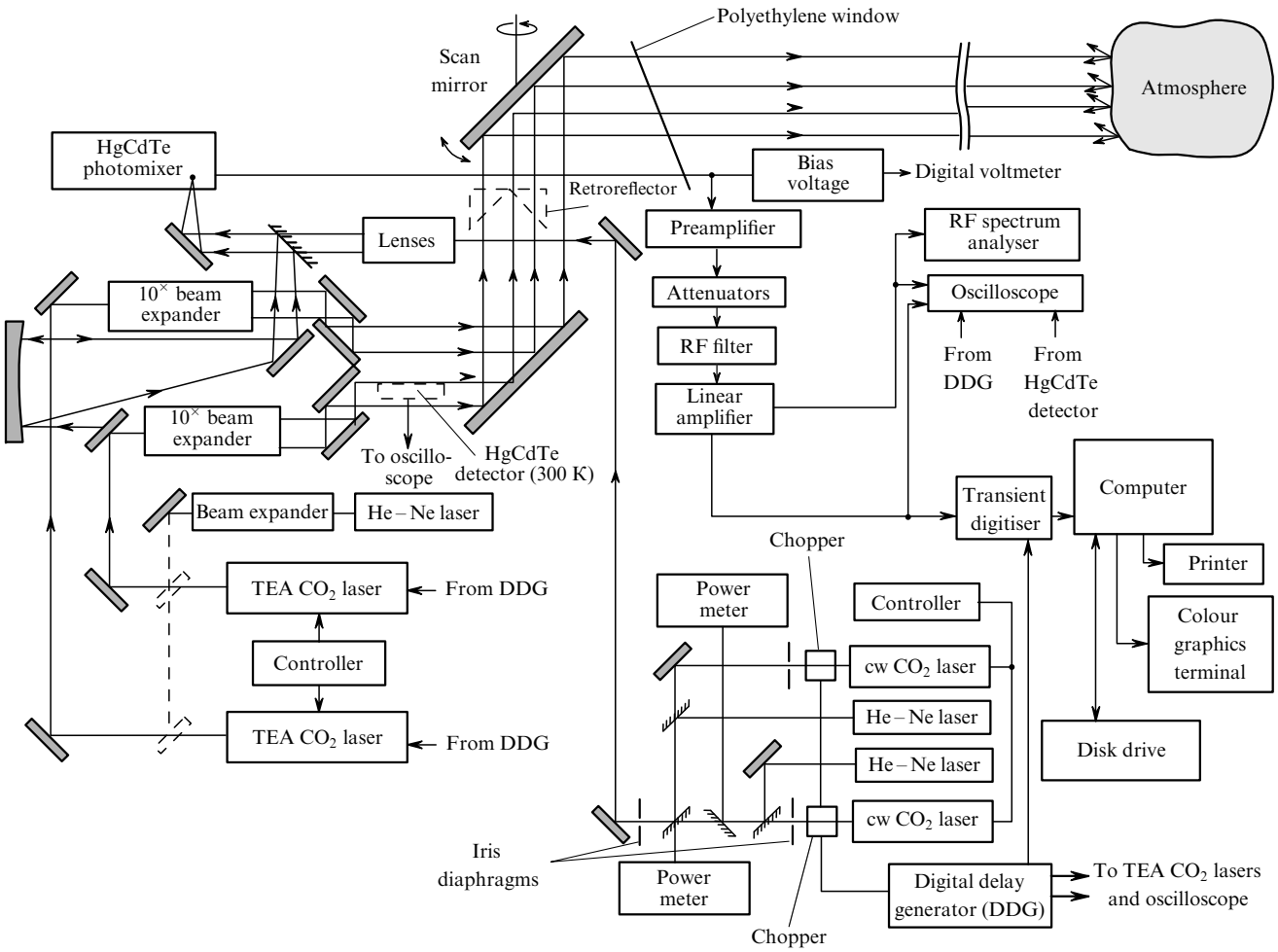

Figure 14. Functional scheme of the MAPM lidar [41]. Dashed lines show replaceable components.

of this mobile lidar showed that the sensing range in the DA regime does not exceed 2–3 km, while in the DA path regime it can achieve 100 km. The matter is that in this spectral range the aerosol backscattering coefficient is very small compared to that in the near-IR range [101, 102], while the sensitivity of detectors is lower by a factor of five (Fig. 8).

In [85], two detection regimes of the CO_2 lidar were studied experimentally. Figure 15 shows the main results of these studies. One can see from Fig. 15a that the sensing range in the direct-detection regime does not exceed 1 km, while in the heterodyne regime it achieves 10 km. The results presented in Fig. 15a were obtained upon DA lidar sensing of ethylene by 100-mJ, 10.532-μm pulses from a TEA CO_2 laser. One can see from Fig. 15 that the lidar sensitivity in the direct-detection regime is much higher than that upon heterodyne detection because of the strong influence of the speckle noise in the latter case.

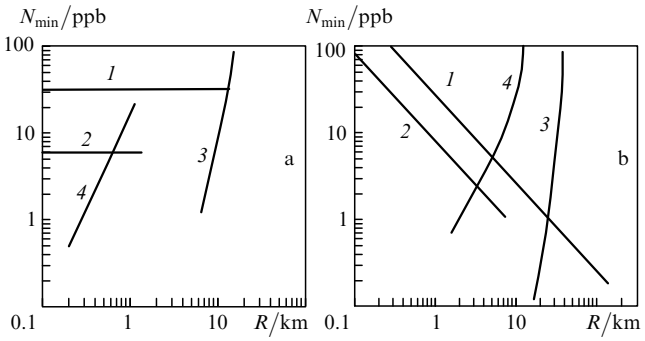

Figure 15. Sensitivity of the DA CO_2 lidar operating in the lidar (a) and path (b) regimes in the case of the heterodyne (*1*) and direct (*2*) detection [85]. Curves (*3*) and (*4*) are the limiting sensitivities restricted by the lidar noise.

The sensing range in the DA path method (Fig. 15b) upon heterodyne detection exceeds 20 km, while in the direct-detection regime it does not achieve 3 km. The difference in the sensitivities for these two detection regimes is not significant.

4.2.4. NH_3 lidars

Until recently a high-power CO_2 laser emitting in the spectral range between 9 and 11 μm was used for lidar sensing of atmospheric ammonia, ozone and a number of other substances. However, the absorption spectra of many pollutants are located in longer-wavelength spectral region between 11 and 18 μm, where the CO_2 laser has no lines. The ammonia–nitrogen laser developed at the Department of Quantum Radiophysics at Lebedev Physics Institute, RAS emits in the spectral region up to 14 μm [136].

The $NH_3 - N_2$ laser belongs to the class of laser-pumped molecular IR lasers. In these lasers, the population inversion

is produced on the vibration – rotation levels of active molecules pumped by another laser. At high gas pressures, lasing can occur simultaneously at many transitions. In this case, the rotational sublevels of the excited vibrational state are populated due to fast rotational relaxation caused by collisions of active molecules with buffer gas molecules and, hence, it is possible to perform laser tuning. The $NH_3 - N_2$ laser is pumped by a pulsed TEA CO_2 laser whose emission spectrum is presented in Fig. 10. The active medium is ammonia $^{14}NH_3$. The addition of nitrogen as a buffer gas provides lasing at many transitions in the range from 745 to 928 cm^{-1} with the conversion efficiency up to 25 % [136]. Figure 16 shows the emission spectrum of this laser, which is the highest-power ammonia laser at present. Table 12 presents the emission parameters of the NH_3 laser [136].

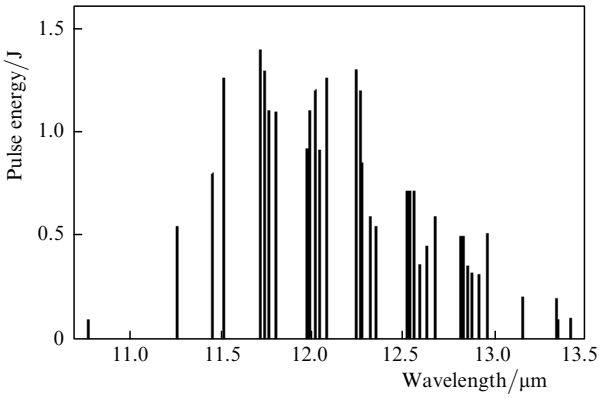

Figure 16. Emission spectrum of the $NH_3 - N_2$ laser [136].

The ammonia laser has a narrow linewidth, which is important for sensing of the atmosphere. The gain linewidth of the ammonia laser is described by the expression $\Delta\nu = 28p_{NH_3} + 3.8p_{N_2}$ [137], where $\Delta\nu$ is measured in megahertz and p_i in Torr. For the optimal active mixture of the ammonia laser $NH_3 : N_2 = 1 : 75$ and a total pressure of 60 Torr, we obtain $\Delta\nu = 247$ MHz. Note for comparison that the gain linewidth of the TEA CO_2 laser varies within 3 – 4 GHz depending on the mixture composition and pressure.

The use of the ammonia laser in lidars was first proposed in [138]. Later, the authors of [139] considered a lidar based on a nonselective-resonator NH_3 laser emitting simultaneously several lines in the range from 11 to 13 μm, which is undoubtedly the advantage of this lidar. However, the number of laser lines in this lasing regime is limited and the energy of each of the lines is several times lower than that for a selective-resonator laser, which restricts the number of gases that can be detected and reduces the sensing range of the lidar. In [140], another optical scheme of a two-frequency ammonia lidar was proposed. However, the system for spatial combining of laser beams had a number of drawbacks making the scheme rather inconvenient, especially in the case of mobile lidars. This problem was solved [141] by using a new optical scheme of a two-frequency ammonia laser in which the output laser beams, including the reference beam [the 9R(30) lines] were collinear and could be simpler controlled than in schemes [138 – 140].

To cover the spectral range between 9 and 13.5 μm, a new optical scheme of a two-frequency radiation source based on CO_2 and NH_3 lasers was proposed [135]. The optical scheme of the NH_3-CO_2 lidar is presented in Fig. 17. The resonator of the NH_3 laser is formed by mirrors M3 and M4 coupled through the zero order of diffraction grating DF3. The NH_3 laser is tuned by rotating mirror M5. The CO_2 laser is tuned by rotating diffraction grating DF2. Beamsplitter B2 is a 1-mm thick plane – parallel silicon plate. Diffraction grating DF1 determines the reference radiation frequency. The laser emission ranges can be switched over from 11 – 13.5 μm to 9 – 11 μm and back by inserting or removing mirror M3.

Table 13 presents known Freons having absorption bands within the emission range of the ammonia laser, the optimal laser lines for their sensing, and the absorption coefficients of these Freons at these lines [35]. Note that Freon 11 and Freon 12 also absorb in the emission range of a CO_2 laser and were sensed with a DA CO_2 lidar [99]. However, their absorption coefficients in this range are four times lower than in the emission range of the ammonia laser [35]. Figure 18 and 19 present the absorption spectra of Freon 11 in the emission regions of the CO_2 and ammonia

Table 12. Radiation parameters of the NH_3 laser [136].

Frequency/cm^{-1}	λ/μm	Transition	Pulse energy/J	Efficiency (%)
891.885	11.21221	aP(2, 1)	0.1	2
888.0779	11.26027	sP(4, *k*)	0.55	8
872.5667	11.46044	aP(3, 1)	0.8	12
–	–	aP(3, 2)	–	–
868.0003	11.52073	sP(5, *k*)	1.25	19
853.8186	11.71209	aP(4, 0)	1.4	21
–	–	aP(4, 1)	–	–
852.7239	11.72713	aP(4, 2)	1.3	20
851.3271	11.74637	aP(4, 3)	1.1	17
847.8756	11.79418	sP(6, *k*)	1.1	17
834.823	11.97859	aP(5, 1)	0.9	14
834.0112	11.99025	aP(5, 2)	1.1	17
832.6338	12.01008	aP(5, 3)	1.2	18
830.6533	12.03872	aP(5, 4)	0.9	14
827.8748	12.07912	sP(7, *k*)	1.25	19
816.6459	12.24521	aP(6, 0)	1.3	20
–	–	aP(6, 1)	–	–
815.5911	12.26105	aP(6, 2)	1.2	18
814.2418	12.28136	aP(6, 3)	0.85	13
812.3002	12.31072	aP(6, 4)	0.6	9
809.7151	12.35002	aP(6, 5)	0.55	8
798.2239	12.52781	aP(7, 1)	0.7	11
797.4491	12.53999	aP(7, 2)	0.7	11
796.1347	12.56069	aP(7, 3)	0.7	11
794.2444	12.59058	aP(7, 4)	0.35	5
791.7261	12.63063	aP(7, 5)	0.45	7
788.5112	12.68213	aP(7, 6)	0.6	9
780.5523	12.81144	aP(8, 0)	0.5	7
–	–	aP(8, 1)	–	–
779.5657	12.82766	aP(8, 2)	0.5	7
778.2932	12.84863	aP(8, 3)	0.35	5
776.4637	12.8789	aP(8, 4)	0.3	5
774.0264	12.91946	aP(8, 5)	0.3	5
770.913	12.97163	aP(8, 6)	0.5	7
760.6919	13.14593	aP(9, 3)	0.2	4
753.5922	13.26978	aP(9, 6)	0.2	4
749.8612	13.3358	aP(9, 7)	0.1	2
745.2938	13.41753	aP(9, 8)	0.1	2

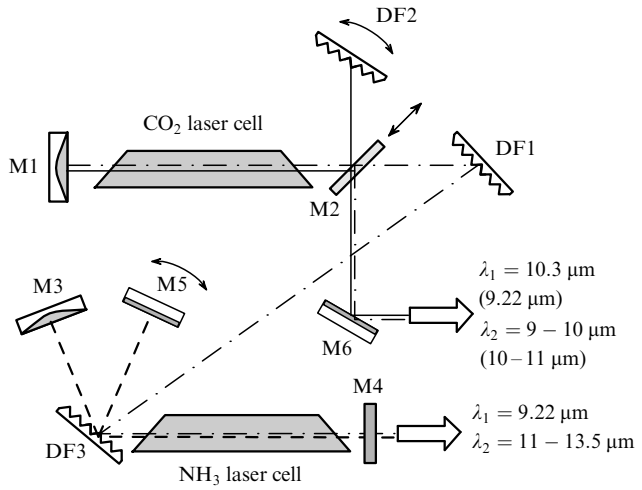

Figure 17. Optical scheme of the NH_3-CO_2 lidar [135]: M1 – M6: mirrors; DF1 – DF3: diffraction gratings; λ_1 and λ_2: wavelengths of the reference and measuring beams, respectively.

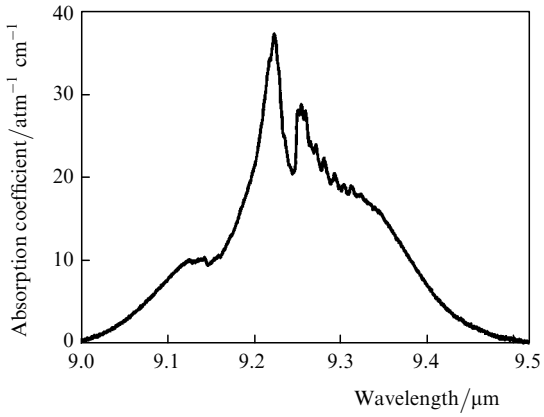

Figure 18. Absorption spectrum of Freon 11 in the emission region of the CO_2 laser [35].

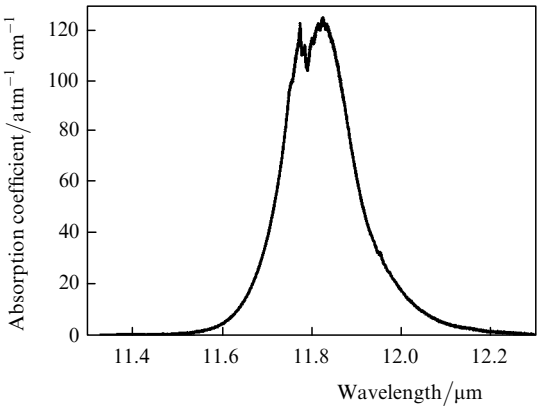

Figure 19. Absorption spectrum of Freon 11 in the emission region of the NH_3 laser [35].

lasers, respectively. A comparison of these spectra shows that the sensing of Freon 11 by the DA ammonia lidar is more efficient that that by a CO_2 lidar.

The optimal parameters of the NH_3-CO_2 lidar with technical parameters presented below were estimated in [137]. According to the estimates, the sensing range of the NH_3-CO_2 lidar changes within 2.5 – 10 km depending on the laser line used in measurements and the state of the atmosphere. The high absorption cross sections of Freon 11 at the lines of the ammonia laser provide a high detection sensitivity, down to 0.4 ppb km. The analysis of sensing errors shows that the concentration of Freon 11 can be measured at the 50 ppb level at distances from 5 to 8 km with a spatial resolution of 150 m.

The NH_3-CO_2 lidar provides a high detection sensitivity (~ 6 ppb) for many substances (Freons, toxins, organic gases, and toxic compounds). The possibility of detecting many molecules, including halogen-substituted hydrocarbons, by means of the NH_3-CO_2 lidar is demonstrated in Table 14 where the absorption lines of these substances are presented [138].

In [142], the possibility of using known IR lasers (CO_2, DF, HF, NH_3, N_2O, and CO lasers) for detecting and identification of 38 substances with absorption spectra taken from the HITRAN-97 atlas was theoretically investigated. It was shown that the NH_3 and CO laser are most optimal for this purpose.

Table 13. Freons, their absorption bands in the emission region of the ammonia laser [35], optimal lines for their sensing, and the corresponding absorption coefficients [137].

Gas	Absorption band/μm	NH_3 laser line	Absorpton coefficient/atm^{-1} cm^{-1}
Freon 11(CCl_3F)	11.364 – 12.346	sP(6, *k*)	115.7
Freon 12 (CCl_2F_2)	10.526 – 11.765	aP(3, 1)	6.55
Freon 13 ($CClF_3$)	12.423 – 13.072	aP(7, 4)	5.77
Freon 21 ($CHCl_2F$)	11.905 – 12.739	aP(6, 3)	25.11
Freon 22 ($CHClF_2$)	11.628 – 13.158	aP(6, 0)	17.64
Freon 113 ($C_2CL_3F_3$)	10.050 – 12.812	aP(6, 2)	36.35
Freon 114 ($C_2Cl_2F_4$)	11.628 – 12.270	aP(4, 0)	22.52
Freon 123 (CF_3CHCl_2)	11.111 – 13.515	aP(5, 2)	16.09
Freon 124 ($CHClF_2CF_3$)	10.869 – 12.657	aP(6, 4)	5.53
Freon 125 (CHF_2CF_3)	11.236 – 11.905	sP(5, *k*)	11.3
Freon 141 (CH_3CCl_2F)	12.658 – 14.085	aP(9, 6)	27.26
Freon 142 (CH_3CClF_2)	7.905 – 11.429	sP(4, *k*)	6.4
Freon 143 (CF_3CH_3)	9.525 – 13.334	aP(5, 4)	3.58
Freon 152 (CH_3CHF_2)	10.050 – 11.905	aP(7, 1)	2.74
Freon 225 ($CClF_2CF_2CHClF$)	11.561 – 14.389	aP(5, 1)	11.13

	CO_2 laser	NH_3 laser
Radiation source		
Spectral range/μm	9 – 11	11 – 13.5
Pulse energy/J	up to 5	up to 1.5
Pulse duration/μs	1	
Divergence behind the beam expander/mrad	0.8	
Beam diameter at the expander output/cm	10	
Expander efficiency (%)	70	
Newton telescope		
Diameter/cm	40	
Focal distance/m	1	
Field of view/mrad	1	
Distance between laser axes and the telescope/cm	50	
Efficiency (%)	80	
CMT detector cooled down to 77 K		
Receiving area/mm	0.5×0.5	
Detection ability/cm $Hz^{1/2}$ W^{-1}	2×10^{11}	
Filter transmission bandwidth/nm	4	
Electronic passband/MHz	1	
Efficiency (%)	50	
Time constant/ns	$\leqslant 10$	

Table 14. Some molecules, including molecules of halogen-substituted hydrocarbons, detected by the NH_3–CO_2 lidar and the laser lines suitable for their detection [138].

Molecule	Vibrational mode	Vibrational frequency/cm^{-1}	Laser transition	Gas	Laser frequency/cm^{-1}
CH_3I	ν_6	882.5	sP(4, *k*)	NH_3	881.1
CH_2Br	ν_7	810	aP(6, 5)	NH_3	809.7
CHF_2Cl	ν_4	812	aP(6, 4)	NH_3	812.0
$CHCl_3$	ν_5	774	aP(8, 5)	NH_3	774.0
CF_4	$\nu_2 + \nu_4$	1076	9R(16)	CO_2	1076
CF_3Cl	ν_2	781	aP(8, 1)	NH_3	780.4
CF_2Cl_2	$\nu_3 + \nu_5$	780	aP(8, 1)	NH_3	780.4
CF_2ClBr	ν_2	872	aP(3, 1)	NH_3	872.6
CF_2Br_2	ν_8	831	aP(5, 4)	NH_3	830.2
CF_2NCl	ν_4	771	aP(8, 6)	NH_3	770.9
$CFCl_3$	ν_4	847	sP(6, *k*)	NH_3	847.4
$CFCl_2Br$	ν_2	796	aP(7, 3)	NH_3	796.0
CCl_4	ν_3	796	aP(7, 3)	NH_3	796.0
Cl_2CNCl	ν_3	746	aP(9, 8)	NH_3	745.3
NO_2	ν_2	756.8	–	NH_3	–
SO_2	$\nu_3 - \nu_2$	854.07	aP(4, 0)	NH_3	853.6
N_2O_3	ν_4	773	aP(8, 5)	NH_3	774.0
N_2O_5	ν_{13}	860	–	NH_3	–
H_2SO_4	ν_4	834	aP(5, 2)	NH_3	834.0
CS_2	$\nu_1 + \nu_2$	1070.97	–	CO_2	–
SO_3	ν_1	1068	–	CO_2	–
CCl_3Br	ν_4	775	aP(7, 3)	NH_3	796.0
$CClBr_3$	ν_1	745	aP(9, 8)	NH_3	745.3

5. Conclusions

The IR DA lidar is the most efficient tool for sensing of atmospheric pollutants such as NH_3, C_2H_2, H_2O, O_3, CO_2, N_2O, HNO_3, SF_6, OSC, CS_2, Freons, organic gases, hydrazine, rocket fuels, and war toxic gases.

The combined use of IR and Raman lidars considerably increases the measurement accuracy because the Raman lidar allows the simultaneous measurement of the profiles of backscattering and extinction coefficients and temperature, which is important for reliable DA measurements of the gas concentration, especially in the troposphere.

The $Ti:Al_2O_3$ laser has unique properties, which distinguish it from other near-IR lasers. Recently this laser has received wide applications, and the fundamental and second-harmonic radiation of this laser is now being used in most near-IR lidars for sensing of water vapour, aerosols, and some atmospheric pollutants.

The NH_3–CO_2 lidar is the most promising IR lidar for monitoring of the environment in the mid-IR region. The emission spectrum of this laser covers the range from 9 to 13.5 μm in which intense absorption bands of many Freons and organic and toxic gases are located.

References

1. Zuev V.E., Zuev V.V. *Distantsionnoe opticheskoe zondirovanie atmosfery* (Remote Optical Sensing of the Atmosphere) (St. Petersburg: Gidrometeoizdat, 1992).
2. Measures R.M. *Laser Remote Sensing: Fundamentals and Applications* (New York: Wiley, 1984; Moscow: Mir, 1987).
3. Hinkley E.D. (Ed.) *Laser Monitoring of the Atmosphere* (New York: Springer-Verlag, 1976; Moscow: Mir, 1979).
4. Browell E.V. *Opt. Eng.*, **21**, 128 (1982).
5. Sakai T., Shibata T., Iwasaka Y. *J. Meteorol. Soc. Jpn*, **75**, 1179 (1997).
6. Bisson S.E., Goldsmith J.E., Mitchell M.G. *Appl. Opt.*, **38**, 1841 (1999).
7. Andreev Yu.M. et al. *Opt. Atmos. Okean.*, **16**, 783 (2003).
8. Fujii T., Futuchi T., Goto N., Nemoto K., Takeuchi N. *Appl. Opt.*, **40** 949 (2001).
9. Rodriguez M., Bourayou R., Kasparian J., et al. *Proc. SPIE Int. Soc. Opt. Eng.*, **5149**, 135 (2003).
10. Mejean G., Kasparian J., et al. *Appl. Phys. B*, **78**, 535 (2004).
11. Abramochkin A.I. et al. *Opt. Atmos. Okean.*, **12**, 345 (1999).
12. Kaul' B.V. *Opt. Atmos. Okean.*, **2**, 211 (1989).
13. Abramochkin A.I., Tikhomirov A.A. *Opt. Atmos. Okean.*, **11**, 899 (1989).
14. Abramochkin A.I. et al. *Opt. Atmos. Okean.*, **12**, 643 (1999).
15. Tikhomirov A.A. *Opt. Atmos. Okean.*, **12**, 208 (2000).
16. Vesselovskii I.A. et al. *Appl. Opt.*, **41**, 3685 (2002).
17. Whiteman D.N., Melfi S.H. *Proc. IX ARM Science Team Meeting* (San Antonio, Texas, 1999).
18. Bissonette L.R., Hutt D.L. *Appl. Opt.*, **34**, 6959 (1995).
19. Van de Hulst H.C. *Light Scattering by Small Particles* (New York: JWS Inc., 1957).
20. Ivlev L.S. Andreev S.D. *Opticheskie svoistva atmosfernykh aerozolei* (Optical Properties of Atmospheric Aerosols) (Leningrad: Leningrad State University, 1986).
21. Sugimoto N. *Opt. Rev.*, **6**, 235 (2000).
22. Whiteman D.N., Melfi S.H., Ferrare R.A. *Appl. Opt.*, **31**, 3068 (1992).
23. Whiteman D.N., Melfi S.H. *Proc. IX ARM Science Team Meeting* (San Antonio, Texas, 1999).
24. Melfi S.H., Evans K.D., et al. *Appl. Opt.*, **36**, 3551 (1997).
25. Ansmann A., Riebesell M., et al. *Appl. Phys. B*, **55**, 18 (1992).
26. Bissonette L.R., Hutt D.L. *Appl. Opt.*, **34**, 6959 (1995).
27. Bissonnette L.R. et al. *Appl. Phys. B*, **60**, 355 (1995).
28. Grant W.B. *Opt. Eng.*, **30**, 40 (1991).
29. Higdon N.S., Browell E.V., et al. *Appl. Opt.*, **33**, 6422 (1994).
30. Wulfmeyer V. *Appl. Opt.*, **37**, 3804 (1998).
31. Behrendt A., Wulfmeyer V. *Proc. SPIE Int. Soc. Opt. Eng.*, **5154**, 61 (2003).
32. Ferrare R. et al. *Proc. SPIE Int. Soc. Opt. Eng.*, **5154**, 52 (2003).
33. Zuev V.V., Kataev M.Yu. et al. *Opt. Atmos. Okean.*, **8**, 1137 (1995).
34. Mayer A., Comera J., Charpentier H., Jaussaud C. *Appl. Opt.*, **17**, 391 (1978).
35. Rothman L.S. et al. *J. Quant. Spectr. Rad. Transfer*, **82**, 5 (2003).

36. Jacquinet-Husson N. et al. *J. Quant. Spectr. Rad. Transfer*, **62**, 205 (1999).
37. Mitsel' A.A. *Opt. Atmos. Okean.*, **5**, 978 (1992).
38. Kataev M.Yu., Mitsel' A.A. *Opt. Atmos. Okean.*, **5**, 979 (1992).
39. Andreev Yu.M. Zuev V.V., Romanovskii O.A. Dep. VINITI, No. 4058-B88, 25.05.88.
40. Futuchi T., Fujii T., Goto N., Nemoto K., Takeuchi N. *Opt. Eng.*, **40**, 392 (2001).
41. Grant W.B. et al. *Appl. Opt.*, **26**, 3033 (1987).
42. Kovalev V.A., Eichinger W.E. *Elastic Lidar: Theory, Practice and Analysis Methods* (New York: JWS Inc., 2004).
43. Sasano Y., Browell E.V., Ismail S. *Appl. Opt.*, **24**, 3929 (1985).
44. Parameswaran K.K. et al. *Appl. Opt.*, **30**, 3059 (1991).
45. Zuev V.E., Krekov G.M. *Opticheskie modeli atmosfery* (Optical Models of the Atmosphere (Leningrad, Gidrometeoizdat, 1986).
46. Klett J.D. *Appl. Opt.*, **20**, 211 (1981).
47. Klett J.D. *Appl. Opt.*, **24**, 1638 (1985).
48. Kovalev V.A. *Appl. Opt.*, **32**, 6053 (1993).
49. Nebuloni R. *Appl. Opt.*, **44**, 3795 (2005).
50. Velotta R., Bartoli B., et al. *Appl. Opt.*, **37**, 6999 (1998).
51. Halldorsson T., Langerholc J. *Appl. Opt.*, **17**, 240 (1978).
52. Harms J., Lahmann W., Weitkamp C. *Appl. Opt.*, **17**, 1131 (1978).
53. Harms J. *Appl. Opt.*, **18**, 1559 (1979).
54. Young S.A. *Appl. Opt.*, **26**, 1612 (1987).
55. Sassano Y., Shimizu H., Takeuchi J., Okuda M. *Appl. Opt.*, **18**, 3908 (1979).
56. Dho S.W., Park Y.J., Kong H.J. *Appl. Opt.*, **36**, 6009 (1997).
57. Kataev M.Yu. *Opt. Atmos. Okean.*, **14**, 782 (2001).
58. Ivanov A.P., Bril' A.I., et al. *Opt. Atmo. Okean.*, **13**, 154 (2000).
59. Aref'ev V.N., Bugrim G.I., Visheratin K.N. *Izv. Ross. Akad. Nauk, Ser. Fiz. Atmos. Okean.*, **28**, 391 (1992).
60. Staeher W., Lahmann W., Weitkamp C. *Appl. Opt.*, **24**, 1950 (1985).
61. Zuev V.V., Romanovskii O.A. Dep. VINITI, No. 4675-B87, 25.06.87.
62. Schotland R.M. *J. Appl. Meteorol.*, **13**, 71 (1974).
63. Andreev Yu.M., Voevodin V.G., Gribenyukov A.I., et al. *Zh. Prikl. Spektr.*, **47**, 15 (1987).
64. Zuev V.E., Kabanov M.V., et al. *Izv. Akad. Nauk SSSR, Ser. Fiz.*, **52**, 1142 (1988).
65. Bristow M.P. et al. *Appl. Opt.*, **34**, 4437 (1995).
66. Killinger D.F., Menyuk N. *Opt. Lett.*, **6**, 301 (1981).
67. Menyuk N., Killinger D.K. *Appl. Opt.*, **22**, 2690 (1983).
68. Grant W.B., Brothers A.M., Bogan J.R. *Appl. Opt.*, **27**, 1934 (1988).
69. Fastig S., Cohen A. *Appl. Opt.*, **27**, 1939 (1988).
70. Menyuk N., Killinger D.K., Menyuk C.R. *Appl. Opt.*, **21**, 3377 (1982).
71. Harney R.C. *Appl. Opt.*, **22**, 3747 (1983).
72. Milton J.T.M., Woods P.T. *Appl. Opt.*, **26**, 2598 (1987).
73. Menyuk N., Killinger D.K., Menyuk C.R. *Appl. Opt.*, **24**, 118 (1985).
74. Firsov K.M., Kataev M.Yu., et al. *J. Quant. Spectr. Rad. Transfer*, **61**, 25 (1999).
75. Zuev V.V., Matvienko O.A. *Opt. Atmos. Okean.*, **11**, 899 (1998).
76. Megie G., Menzies R.T. *Appl. Opt.*, **19**, 1173 (1980).
77. Moulton P. et al. *Proc. SPIE Int. Soc. Opt. Eng.*, **4893**, 193 (2003).
78. Reid J., Sinclair L., et al. *Opt. Quantum Electron.*, **17**, 31 (1985).
79. Shfrin K.S. *Appl. Opt.*, **34**, 4480 (1995).
80. Cahen C., Megie G. *J. Quant. Spectr. Rad. Transfer*, **25**, 151 (1981).
81. Hansen G.L. et al. *J. Appl. Phys.*, **53**, 7099 (1982).
82. Rein M.B. *Proc. SPIE Int. Soc. Opt. Eng.*, **443**, 2 (1983).
83. Hardesty R.M. *Appl. Opt.*, **23**, 2545 (1984).
84. Roadcap J.R. et al. *Proc. SPIE Int. Soc. Opt. Eng.*, **3127**, 201 (1997).
85. Killinger D.F., Menyuk N., De Feo W.E. *Appl. Opt.*, **22**, 682 (1983).
86. Duarte F.J. *Tunable Lasers: Hand Book* (New York: Acad. Press, 1995).
87. Gorodnichev V.A., Kozintsev V.I. *Opt. Atmos. Okean.*, **7**, 1410 (1994).
88. Menyuk N., Killinger D.K. *Appl. Opt.*, **26**, 3061 (1987).
89. Prasad C.R. et al. *Proc. SPIE Int. Soc. Opt. Eng.*, **3757**, 87 (1998).
90. Ambrico P.F., Amodeo A., et al. *Proc. SPIE Int. Soc. Opt. Eng.*, **3504**, 111 (1998).
91. Agroskin V.Y. et al. *Proc. SPIE Int. Soc. Opt. Eng.*, **5416**, 245 (2004).
92. Philippov P.G. et al. *Proc. SPIE Int. Soc. Opt. Eng.*, **3504**, 119 (1998).
93. Geiger A.R. et al. *Proc. SPIE Int. Soc. Opt. Eng.*, **3380**, 63 (1998).
94. Romanovskii O.A., Kharchenko O.V. *Proc. SPIE Int. Soc. Opt. Eng.*, **5743**, 441 (2004).
95. Lee S.W. et al. *Proc. SPIE Int. Soc. Opt. Eng.*, **3757**, 96 (1999).
96. Prasad N.S., Geiger A.R. *Opt. Eng.*, **35**, 1105 (1996).
97. Hoffland L.D., Piffath R.J., Bouck J.B. *Opt. Eng.*, **24**, 982 (1985).
98. Grant W.G. *Appl. Opt.*, **25**, 709 (1986).
99. Murray E.R. *Opt. Eng.*, **16**, 284 (1977).
100. Rothe K.W. *Radio Electron. Eng.*, **50**, 567 (1980).
101. Schwiesow R.L., Cupp R.E., et al. *J. Appl. Meteorol.*, **20**, 184 (1981).
102. Ben-David A. *Appl. Opt.*, **38**, 2616 (1999).
103. Killinger D.F., Menyuk N. *IEEE J. Quantum Electron.*, **17**, 1917 (1981).
104. Zuev V.E., Makushkin Yu.S., et al. *Appl. Opt.*, **22**, 3733 (1983).
105. Quagliano J.R., Stoutland P.O., et al. *Appl. Opt.*, **36**, 1915 (1997).
106. Force A.P., Killinger D.K., De Feo W.E., Menyuk N. *Appl. Opt.*, **24**, 2837 (1985).
107. Chimelis V. *Appl. Opt.*, **21**, 3367 (1982).
108. Fox J.A., Gautier C.R., Ahi J.L. *Appl. Opt.*, **27**, 847 (1988).
109. Zhao Y. *Appl. Opt.*, **39**, 997 (2000).
110. Karapuzikov A.I. et al. *Opt. Atmos. Okean.*, **12**, 364 (1999).
111. Voitsekhovckaya O.K., Aksenova E.N., Shatrov F.G. *Appl. Opt.*, **38**, 2337 (1999).
112. Persson U., Marthinsson B., Johansson J., Eng S.T. *Appl. Opt.*, **19**, 1711 (1980).
113. Aref'ev V.N. *Kvantovaya Elektron.*, **12**, 631 (1985) [*Sov. J. Quantum Electron.*, **15**, 413 (1985)].
114. Pogodaev V.A. *Opt. Atmos. Okean.*, **6**, 339 (1993).
115. Melngails I., Keicher W.E., et al. *Proc. IEEE*, **84**, 227 (1996).
116. Zhao Y., Hardesty R.M. *Appl. Opt.*, **27**, 2719 (1988).
117. Gautier C.R., Fox J.A., Ahi J.L. *Proc. SPIE Int. Soc. Opt. Eng.*, **1042**, 103 (1989).
118. Fox J., Ahi J. *Appl. Opt.*, **25**, 3830 (1986).
119. Platt C.M.R., Takashima T. *Appl. Opt.*, **26**, 1257 (1987).
120. Nordstrom R.J. *Proc. SPIE Int. Soc. Opt. Eng.*, **902**, 138 (1988).
121. Ivashchenko M.V., Sherstov I.V. *Kvantovaya Elektron.*, **30**, 747 (2000) [*Quantum Electron.*, **30**, 747 (2000)].
122. Pethran J.C. *Appl. Opt.*, **20**, 3941 (1981).
123. Uthe E.E. *Appl. Opt.*, **25**, 2492 (1986).
124. Andreev Y.M., Geiko P.P., Sherstov I.V. *Proc. SPIE Int. Soc. Opt. Eng.*, **3983**, 386 (1999).
125. Karapuzikov A.I., Matvienko G.G., et al. *Proc. SPIE Int. Soc. Opt. Eng.*, **3983**, 476 (1999).
126. Karapuzikov A.I., Sherstov I.V., et al. *Proc. SPIE Int. Soc. Opt. Eng.*, **4063**, 255 (2000).
127. Grant W.B. *Proc. SPIE Int. Soc. Opt. Eng.*, **1062**, 172 (1989).
128. Carlisle C.B., Van der Laan J.E., et al. *Appl. Opt.*, **34**, 6187 (1995).
129. Zuev V.E., Zuev V.V., Makushkin Yu.S., et al. *Appl. Opt.*, **22**, 3742 (1983).
130. Baker P.W. *Appl. Opt.*, **22**, 2257 (1983).
131. Kol'yakov S.F., Malyavkin L.P. *Kvantovaya Elektron.*, **15**, 212 (1988). [*Sov. J. Quantum Electron.*, **18**, 135 (1988)].
132. Murray E.R., Van der Laan J.E. *Appl. Opt.*, **17**, 814 (1978).
133. Menyuk N., Killinger D.K., De Feo W.E. *Appl. Opt.*, **24**, 2837 (1985).
134. Leonelli J., Holland P.L., Van Der Laan J.E. *Proc. SPIE Int. Soc. Opt. Eng.*, **5149**, 203 (1989).

135. Vasil'ev B.I., Zheltukhin A.A., Mannum O.M. *Kratk. Soobshch. Fiz. FIAN*, (7), 22 (2004).
136. Vasil'ev B.I., Grasyuk A.Z., et al. *Kvantovaya Elektron.*, **7**, 116 (1980) [*Sov. J. Quantum Electron.*, **10**, 64 (1980)].
137. Vasil'ev B.I., Mannoun O.M. *Kvantovaya Elektron.*, **35**, 523 (2005) [*Quantum Electron.*, **35**, 523 (2005)].
138. Vasil'ev B.I., Yastrebkov A.B. *Izv. Ross. Akad. Nauk., Ser. Fiz.*, **58**, 202 (1994).
139. Baranov V.Yu., Bobkov I.V., et al. Preprint TRINITI, No. 0043-A (Troitsk, 1998).
140. Anan'ev V.Yu., Vasil'ev B.I., et al. *Kvantovaya Elektron.*, **30**, 535 (2000) [*Quantum Electron.*, **30**, 535 (2000)].
141. Vasil'ev B.I., Cho Chen Vhan. *Kvantovaya Elektron.*, **30**, 1105 (2000) [*Quantum Electron.*, **30**, 1105 (2000)].
142. Ivanov S.V., Ionin A.A. *Proc. SPIE Int. Soc. Opt. Eng.*, **5149**, 161 (2003).